

## Exotic symmetries as stabilizing factors for superheavy nuclei: Symmetry-oriented generalized concept of nuclear magic numbers

J. Yang <sup>1,2</sup>, J. Dudek <sup>3,\*</sup>, I. Dedes <sup>4</sup>, A. Baran <sup>2</sup>, D. Curien <sup>3</sup>, A. Gaamouci <sup>5</sup>, A. Gózdź <sup>2</sup>,  
A. Peđrak <sup>6</sup>, D. Rouvel <sup>3</sup> and H. L. Wang <sup>1</sup>

<sup>1</sup>*School of Physics and Microelectronics, Zhengzhou University, Zhengzhou 450001, China*

<sup>2</sup>*Institute of Physics, Marie Curie-Skłodowska University, PL-20 031 Lublin, Poland*

<sup>3</sup>*Université de Strasbourg, CNRS, IPHC UMR 7178, F-67 000 Strasbourg, France*

<sup>4</sup>*Institute of Nuclear Physics Polish Academy of Sciences, PL-31 342 Kraków, Poland*

<sup>5</sup>*Laboratoire de Physique Théorique, Faculté de Physique, USTHB, BP 32, El Alia, 16111 Bab Ezzouar, Algiers, Algeria*

<sup>6</sup>*National Centre for Nuclear Research, Theoretical Physics Division, PL-02-093 Warsaw, Poland*



(Received 9 August 2022; accepted 1 November 2022; published 14 November 2022)

We introduce the concept of the nuclear octupole fourfold (i.e., applying simultaneously to all the four octupole deformations  $\alpha_{30}$ ,  $\alpha_{31}$ ,  $\alpha_{32}$ , and  $\alpha_{33}$ ) neutron “magic number”  $N = 196$  and discuss the physical consequences of its presence. Our theoretical predictions are obtained using the realistic phenomenological mean-field approach with the deformed Woods-Saxon potential, the latter employing the new parametrization optimized in our preceding articles. Correlations among 4 parameters in the set of 12 parameters of the Woods-Saxon potential are detected and removed employing Monte Carlo approach leading to stabilization of the predictive power of the modeling. Our main focus is examining the impact of the four-fold octupole magic number  $N = 196$  on the stability properties of superheavy nuclei with  $114 \leq Z \leq 130$  and  $166 \leq N \leq 206$ . Calculations suggest that majority of the examined nuclei are either spherical or octupole deformed, octupole-tetrahedral geometry playing the dominating role lowering the ground-state energy by up to 8 MeV. The origin and manifestations of this domination are illustrated and discussed. It turns out that, in several cases, alternative point-group symmetries may lead to noticeable lowering of the nuclear energy; this concerns the  $C_{2v}$  geometry associated with  $\alpha_{31}$ , the  $D_{3h}$  geometry related to  $\alpha_{33}$ , and  $D_{2d}$  corresponding to the combination of  $\alpha_{32}$  and  $\alpha_{20}$  quadrupole component.

DOI: [10.1103/PhysRevC.106.054314](https://doi.org/10.1103/PhysRevC.106.054314)

### I. INTRODUCTION

One of the most fundamental questions about atomic nuclei concerns the limits of existence of nuclear systems, which can be found in nature or produced in the laboratory. Nuclei at those limits are usually referred to as exotic. Particular questions concern the biggest proton and/or neutron numbers leading to sufficiently long-lived nuclear systems, which could be identified and studied. These latter nuclei are traditionally called “superheavy.” Attempts to synthesize so-far unknown elements beyond uranium were undertaken already in the early 1930s. However, only 278 nuclei among about 3000 known today experimentally can be found in nature, cf. Ref. [1].

#### A. Symmetries and the notion of magic numbers

To present the impact of selected symmetries on the nuclear stability—here we consider selected geometrical ones—it will be of certain interest to clarify the mathematical background and generality, both hidden in the historical notion of nuclear stability expressed by employing the language

of “magic” numbers. Such a name left without a comment might leave the impression that one is talking about some unexpectedly big shell effects appearing incidentally “here and there”—wherefrom the name “magic.” In reality, we are dealing with perfectly defined quantum circumstances, which can be specified and generalized to *various* contexts, e.g., of symmetries.

This broadly used terminology was centered around the word “magic,” taking origin in pioneering works of Goeppert-Mayer, Wigner, and Jensen which resulted in their common Nobel Prize in 1963. These authors succeeded in linking properties of specific spatial configurations of the nucleonic densities and resulting nuclear stability. They revealed on this occasion the premier role of the nuclear spin-orbit interaction potential played in their particular case. Using the terminology of the closed spherical shells and the formalism of the orbital,  $\hat{\ell}$ , intrinsic,  $\hat{s}$ , and total,  $\hat{j} \equiv \hat{\ell} + \hat{s}$ , nucleonic angular momenta they were able to associate an increased nuclear stability—measured by sufficiently large gaps in the corresponding energy spectra—with the numbers of nucleons in the nucleus corresponding to the expulsion of the highest- $\ell$  orbital from its proper main  $\mathcal{N}$  shell to the  $(\mathcal{N} - 1)$  shell below (intruder states). These were the special values of those numbers of nucleons, sometimes referred to as nucleonic

\*Corresponding author: jerzy.dudek@iphc.cnrs.fr

occupation numbers, which were attached to the locally strongest binding, and on this occasion attributed the appellation “magic numbers.”

Of course, from the quantum mechanics viewpoint there are no “magic tasks” performed. One singles out an interaction potential, in the discussed historical case the spin-orbit:

$$\hat{V}_{\ell,s} \propto \hat{\ell} \cdot \hat{s}, \quad (1)$$

which, with the help of the quantum state labeling by  $\ell$ ,  $s$ , and  $j$  identifies the parallel or antiparallel couplings ( $\vec{\ell} \uparrow \uparrow \vec{s}$ ) as opposed to ( $\vec{\ell} \uparrow \downarrow \vec{s}$ ). From now on it is sufficient to record variations of the gaps in the single-particle spectra with the occupation numbers and baptize as “magic” those which provide the maximum energy gaps.

Let us notice that arguments followed so far were dealing with the possibly simplest geometrical context: the stability of *spherical* symmetry configurations within closed *spherical shells*. Is this the condition *sine qua non*? Can the same (appropriately defined) magic number describe more than one physics contexts, such as, for instance, several *distinct* geometrical symmetries? Or, following some other gap-selection criteria not related with any symmetry at all? Since the answers are affirmative and we are interested in some such cases in the present article, we wish to add some more precision as it seems appropriate in the context.

With this goal in mind we will try to present arguments in a general manner by making abstraction from the intruder orbital context exploited in the originally mentioned case. Indeed, what has been done in the historical example of spin-orbit interaction and what will need to be done in any new context is the following:

- (1) We need to identify or define a certain interaction term of specific interest in the Hamiltonian, and
- (2) We need to relate the size of the single-particle level spacing impacted by this interaction term to the occupation numbers and obtain the experiment-comparable output.

In other words, the “occupation numbers” associated with the new phenomena can still be called magic numbers to follow the long years of tradition—but this time representing a totally different physics content. To complete the definition of the new context adapted to our project in this article, we propose the following replacements in terms of terminology:

First, the spin-orbit potential will be replaced by a model potential representing nuclear long-range multipole-multipole interactions, i.e.,  $\hat{V}_{Q,Q}$  replacing  $\hat{V}_{\ell,s}$ :

$$\hat{V}_{\ell,s} \propto \hat{\ell} \cdot \hat{s} \rightarrow \hat{V}_{Q,Q} \propto \hat{Q}_{\lambda=3}^{\dagger} \otimes \hat{Q}_{\lambda=3}. \quad (2)$$

Second, since we are going to be interested in the octupole (multipolarity  $\lambda = 3$ ) shape generated structures, the condition on the orbital angular-momentum quantum numbers for the “bra” and “ket” states to couple will be

$$\hat{\ell} \uparrow \uparrow \hat{s} \rightarrow \Delta \ell = 3 \text{ and } \Delta j = 3. \quad (3)$$

Third, the long past history magic numbers 8, 20, 28, 50, 82, and 126 will be replaced by the occupation numbers

realizing the biggest gaps among the single-particle spectra under nonzero octupole deformations  $\alpha_{3\mu} \neq 0$ .

We believe that it will inspire imagination to introduce a new notion of magicity in nuclear structure applying in many different contexts. For instance, in the present case this is the magic number, say  $N$ , applying to more than one observable at the time (here four times within four types of geometries with deformations  $\alpha_{30}$ ,  $\alpha_{31}$ ,  $\alpha_{32}$ , and  $\alpha_{33}$ , in place of the single—spherical—geometry.) Incidentally, all the listed cases generate five different (nuclear shape) point-group symmetries represented by one “universal” magic number: here— $N = 196$ .

## B. Overview of the past research as the background for the present project

Among leading mechanisms limiting nuclear existence we find the one of nucleonic binding: As soon as the neutron and/or proton separation energies approach zero,  $B_{n/p} \rightarrow 0$ , the stability of the implied systems gets impacted by particle emission and associated decreasing or vanishing lifetimes.

Another limitation is related to the balance between the Coulomb repulsion among the protons and the overall nuclear binding. Both of these combined, determine the heights of the nuclear fission barriers. Vanishing of those barriers,  $B_f \rightarrow 0$ , leads to vanishing of nuclear resistance to fission and thus stability. In other words: With the fission barriers tending to zero, the nucleus can fission within very short fission lifetimes down to  $T \approx 10^{-19}$  s, whereas the limit of the existence of the chemical elements defined by the spontaneous fission is about  $T \approx 10^{-14}$  s, according to Ref. [2], cf. also references therein.

On the contrary, nuclear stability against specific decay modes might significantly increase thanks to quantum symmetries since each symmetry can generate its own decay-hindrance factors. Thus in case of competition between the nuclear configurations not involving and involving symmetries, these are the latter ones which offer potentially broader horizons, and their studies can become primordial for identification of superheavy nuclei. By employing theory methods and predicting possible presence of symmetries in various areas of the nuclear chart, we might be able to formulate optimal conditions for experimental research and successful identification of new, possibly more and more exotic structures.

Let us notice that geometrical symmetries are going to influence directly also the two elementary mechanisms limiting the nuclear stability remarked above. On the one hand, the nucleonic binding is directly associated with the nuclear deformation and thus will vary when the nuclear shapes will follow a certain stabilizing shell effect. This may slow down or accelerate particle emission. Similar things can be said about the variation of the form of the fission barriers depending on the actual nuclear equilibrium and the corresponding shape.

Following this way of reasoning, which encourages examining symmetries, in Ref. [3] a universal mechanism inducing the presence of a number *exotic geometrical symmetries* in several nuclei in the Pb- and light-actinide regions was established and discussed in detail. These symmetries successfully

compete with those resulting from traditional “prolate-oblate quadrupole shape coexistence” studied for a long time in the past.

Let us note in passing that, in this article, we refer to nuclear shape symmetries as *exotic* if

- (1) they do not coincide with well-known quadrupole or axial octupole (pear shape) symmetries, and
- (2) they can formally be described by one of the point-group (also called “molecular”) symmetries.

It turns out that the mechanism examined in Ref. [3] generates a number of exotic geometrical symmetries, such as the recently discovered tetrahedral symmetry,  $T_d$ , Ref. [4], see also references therein, and three other symmetries,  $C_{2v}$ ,  $D_{2d}$ , and  $D_{3h}$ . The description of this mechanism has been formulated by using the nuclear mean-field terminology of magic numbers and related shell effects. More precisely, using the most recent parametrization of the phenomenological realistic nuclear mean field, the authors of the above reference derive the presence of an octupole magic number  $N = 136$  with significant single-particle energy gaps occurring simultaneously for all the four octupole deformations,  $\alpha_{30}$ ,  $\alpha_{31}$ ,  $\alpha_{32}$ , and  $\alpha_{33}$ , wherefrom the name *universal octupole magic number*  $N = 136$ .

In the present article we generalize and extend arguments applied to the Pb and light-actinide regions of Ref. [3] to superheavy nuclei, for which an analogous *universal octupole magic number* is shown to be  $N = 196$ . Particular selection of superheavy nuclei to be studied in the present article was dictated by the fact that we wish to cover, possibly optimally, the area of the nuclear chart in which the symmetries in question are predicted.

This recent evolution can be compared with the results of calculations of the pear-shape octupole deformation effects in heavy and superheavy nuclei carried out by many authors over the last decades. Within the relativistic Hartree-Fock-Bogolyubov theory, a region of octupole deformation in heavy nuclei around  $Z \approx 98$  and  $N \approx 196$  was predicted, whereas the octupole effects were predicted to be absent in these superheavy nuclei according to Refs. [5–7]. The axial reflection-asymmetric Hartree-Fock-Bogolyubov approach suggested that many neutron-rich actinide nuclei, in particular with  $184 < N < 206$  are pear-shaped in their ground states, cf. e.g., Fig. 4 in Ref. [8], and references therein. In contrast, the existence of octupole deformed nuclei in the superheavy region around  $Z \approx 120$  and  $N \approx 190$  was predicted by the macroscopic-microscopic model in Ref. [9] and the Hartree-Fock-Bogolyubov approach with density-dependent Gogny interactions, Ref. [10]. Moreover, recent macroscopic-microscopic calculations in Refs. [11,12] have shown that the tetrahedral-octupole deformation appears in nuclei with  $Z \approx 98$  and  $N \approx 192$  and  $Z \approx 126$  and  $N \approx 192$ . More generally, these articles argue that octupole deformation in superheavy nuclei occurs at neutron numbers around  $N \approx 190$ .

These observations indicate that there is a rather significant overlap between the range of nuclei addressed in the cited literature and the present study, even though certain structural

mechanism in the focus of our article will also differ in many aspects, as shown later.

In the experimental research addressing superheavy nuclei, the new generation of facilities have served for many years to explore the limits of stability of very heavy and superheavy nuclei. Between 1981 and 1992, the superheavy elements  $Z = 107$ – $112$  were discovered and identified at the GSI laboratories, see Ref. [13] and the references therein, where  $Z = 107$  was the first new synthesized element. Synthesis of the element  $Z = 113$  was successfully completed in the RIKEN laboratory, cf. Ref. [14]. The recent experiments in Dubna have discovered the superheavy nuclei  $Z = 114$ – $118$  and confirmed through hot fusion processes, cf. Refs. [15–18]. Other attempts to produce new elements with  $Z > 120$  were also discussed in Refs. [19–21].

On the theory side, selected global properties could be reproduced by using the liquid drop model, whereas the description of the shell structures, in particular the spherical energy gaps, could be approached by a microscopic description involving mean-field methods, and methods employing nucleon-nucleon interactions, cf., early attempts, e.g., in Ref. [22]. In particular, in Ref. [23], the proton number  $Z = 114$  and neutron number  $N = 184$  were predicted as the next spherical shell closures above the  $Z = 82$  and  $N = 126$  ones. Also, the microscopic self-consistent approaches, such as the self-consistent Skyrme-Hartree-Fock-Bogolyubov approximation within the effective density functional formalism, have been used leading to prediction of the spherical magic numbers at  $Z = 126$  and  $N = 184$  in the superheavy region, cf. Refs. [24,25].

Moreover, studies employing spherical relativistic and nonrelativistic mean-field calculations suggest that the spherical shell gaps occur at  $Z = 114$ ,  $N = 184$ , alternatively  $Z = 120$ ,  $N = 172$  or  $Z = 126$ ,  $N = 184$ , as discussed in Ref. [26]. Early deformed relativistic mean-field calculations predicted possible magic numbers at  $Z = 120$  and  $N = 184$ , cf. Refs. [27,28] and references therein. More recently, Ref. [29], involving up-to-date covariant energy density functionals, studied their impact on the deformation and shell effect evolution in superheavy nuclei. The authors concluded that impact of the spherical gap  $N = 172$  is limited and, instead, important shell effects appear at  $N = 184$ , fully confirmed by the present project, cf. Fig. 5.

More recently, predictions of stabilizing shell effects in superheavy nuclei using the Skyrme-Hartree-Fock approach were extended to so-called hyper-heavy nuclei around  $N = 258$  and  $308$  (where the nuclei with  $Z > 126$  are referred to as hyper-heavy) cf. Ref. [30], and where predictions were based on considerations limited to the shell-energies evaluated at spherical shapes. Within the framework of the covariant density-functional calculations, three regions of the spherical hyper-heavy nuclei: ( $Z \approx 138$ ,  $N \approx 230$ ), ( $Z \approx 156$ ,  $N \approx 310$ ), and ( $Z \approx 174$ ,  $N \approx 410$ ) were predicted, cf. Ref. [31]. This study was extended in Ref. [32] and followed up in Ref. [33], emphasizing the abundance of nuclear toroidal structures for  $Z$  exceeding  $Z \approx 130$ —and analyzing the properties of the predicted structures.

From a global perspective, systematic theoretical studies of the properties of superheavy nuclei were intensively

developed in nuclear physics over the past 70 years or so. The interested reader may find the results with various theoretical approaches presented in several review articles, cf., e.g., Refs. [2,34–38].

## II. MACROSCOPIC-MICROSCOPIC METHOD AND THE PRESENT MEAN-FIELD HAMILTONIAN

In the present article we address problems of existence and stability of selected ( $114 \leq Z \leq 130$  and  $166 \leq N \leq 206$ ) superheavy nuclei within a realistic phenomenological mean-field approach employing the deformed Woods-Saxon potential and the so-called macroscopic-microscopic method. The sections below summarize the leading lines and the basic definitions.

### A. Macroscopic-microscopic method: A summary

Without entering into details addressing the modeling used in this article, let us limit ourselves to merely reminding the reader about certain concepts, definitions, and notation.

The nuclear potential energies are calculated with the help of the macroscopic-microscopic method of Strutinsky, cf. Refs. [39,40], as

$$E_{\text{total}} = E_{\text{macro}} + \delta E_{\text{micro}}^{\pi} + \delta E_{\text{micro}}^{\nu}. \quad (4)$$

The first term represents the classical macroscopic liquid-drop model contribution, whereas the two microscopic terms, each of which contains the so-called shell-correction and pairing correction terms, are defined after Refs. [39,40] for protons and neutrons separately.

The macroscopic energy expression employed in this article is that of the finite-range liquid-drop model (FRLDM) with the surface energy term given by the Yukawa-plus-exponential finite range model, Ref. [41]. It coincides with Eq. (62) of Ref. [9]; otherwise we follow the formulation of Refs. [42,43]. All the concepts of the macroscopic-microscopic approximation can be considered standard; some details related to adaptation to our context can be found in Ref. [44] and the references therein.

### B. Definition and elementary features of the mean-field Hamiltonian

The nuclear mean-field Woods-Saxon Hamiltonian is defined as usual as follows:

$$\hat{\mathcal{H}}_{WS} = \hat{\mathcal{T}} + \hat{\mathcal{V}}_{WS} + \hat{\mathcal{V}}_{WS}^{so} + [\hat{\mathcal{V}}_{\text{Coulomb}} \text{ for protons}], \quad (5)$$

where  $\hat{\mathcal{T}}$  denotes the nucleonic kinetic-energy operator and  $\hat{\mathcal{V}}_{WS}$  is the central Woods-Saxon potential,

$$\hat{\mathcal{V}}_{WS}(\vec{r}, \alpha; V^c, r^c, a^c) = \frac{V^c}{1 + \exp[\text{dist}_{\Sigma}(\vec{r}, R^c; \alpha)/a^c]}. \quad (6)$$

By construction it depends on the nuclear surface  $\Sigma$  and involves:  $V^c$  as the central potential depth parameter,  $r^c$  (in  $R^c = r^c A^{1/3}$ ), the central potential radius parameter, and  $a^c$ , the central-potential diffusivity parameter.

We use the “universal” parametrization of the potential taken from Ref. [44]. The adjective “universal” refers to the fact that the underlying parametrization is applied to all the

nuclei of the nuclear chart without further modifications. The concept of universality evolved during the years of its employment. The *universal Woods-Saxon Hamiltonian* and associated so-called “universal parametrization” has been developed in a series of articles, cf. Refs. [45–48] and summarized in Ref. [49], cf. also Ref. [50] for further illustrations. This approach is being used without modifications by many authors also today.

The function  $\text{dist}_{\Sigma}(\vec{r}, R^c; \alpha)$  defines the geometrical distance between the actual nucleonic position,  $\vec{r} \equiv \{x, y, z\}$ , and the nuclear surface  $\Sigma$ , the latter expressed with the help of the spherical-harmonic basis,  $\{Y_{\lambda\mu}(\vartheta, \varphi)\}$ . Again we employ the standard form of the surface definition:

$$\Sigma: R(\vartheta, \varphi) = R_0 c(\alpha) \left[ 1 + \sum_{\lambda\mu} \alpha_{\lambda\mu}^* Y_{\lambda\mu}(\vartheta, \varphi) \right]. \quad (7)$$

The expansion coefficients  $\alpha_{\lambda\mu}$  are called “deformation parameters” or “deformations.” These parameters can in principle be complex, but in nuclear structure physics one traditionally employs a real realization only. The nuclear surface definition in Eq. (7) contains an extra auxiliary function  $c(\alpha)$ , with the help of which we assure that the volume encompassed by the surface does not depend on deformation.

The third term in Eq. (5) stands for the mean-field spin-orbit potential. By definition, its Woods-Saxon form depends on the gradient of the central potential, with appropriately redefined parameters

$$\hat{\mathcal{V}}_{WS}^{so}(\vec{r}, \hat{p}, \hat{s}, \alpha; \lambda^{so}, r^{so}, a^{so}) = \frac{2\hbar\lambda^{so}}{(2mc)^2} [(\vec{\nabla}V_{WS}^{so}) \wedge \hat{p}] \cdot \hat{s}, \quad (8)$$

where

$$V_{WS}^{so}(\vec{r}, \alpha; V^c, r^{so}, a^{so}) = \frac{V^c}{1 + \exp[\text{dist}_{\Sigma}(\vec{r}, R^{so}; \alpha)/a^{so}]}. \quad (9)$$

This potential depends on three adjustable parameters:  $\lambda^{so}$ , which is a dimensionless spin-orbit strength scaling factor,  $r^{so}$  (in  $R^{so} = r^{so} A^{1/3}$ ), which represents the spin-orbit radius parameter, and  $a^{so}$  serving as the spin-orbit diffusivity parameter.

It follows that the phenomenological, deformed mean-field Woods-Saxon Hamiltonian depends on two sets of parameters,

$$\{V^c, r^c, a^c; \lambda^{so}, r^{so}, a^{so}\}_{\pi, \nu}, \quad (10)$$

the one involving six parameters for protons ( $\pi$ ), and the one with six parameters for neutrons ( $\nu$ ), respectively. Certain authors introduce an alternative representation of the parameters, which explicitly involves a smooth dependence on  $Z$  and  $N$ . This modified representation has been of advantage, in particular when adjusting the mean-field Hamiltonian parameters in Ref. [44] to the empirical single-nucleon energies for a series of doubly magic spherical nuclei

$$^{16}\text{O}, \ ^{40}\text{Ca}, \ ^{48}\text{Ca}, \ ^{56}\text{Ni}, \ ^{90}\text{Zr}, \ ^{132}\text{Sn}, \ ^{146}\text{Gd}, \ ^{208}\text{Pb}, \quad (11)$$

deduced using experimental results compiled in Ref. [51]. More precisely, the smooth dependence on  $Z$  and  $N$  involving the isospin dependence in the central and spin-orbit potential strength parameters introduces directly the isospin strength

constants,  $\kappa^c$  and  $\kappa^{so}$ , so that

$$V_{\pi,v}^c = V_0^c \left( 1 \pm \kappa^c \frac{N-Z}{N+Z} \right) \quad (12)$$

and

$$\lambda_{\pi,v}^{so} = \lambda_0^{so} \left( 1 \pm \kappa^{so} \frac{N-Z}{N+Z} \right), \quad (13)$$

with the plus sign for the protons and the minus sign for the neutrons. The modified parametrization involves  $V_0^c$ ,  $\lambda_0^{so}$  as well as  $\kappa^c$  and  $\kappa^{so}$  as the new adjustable constants:

$$\{V_0^c, \kappa^c; \lambda_0^{so}, \kappa^{so}\} \leftrightarrow \{V_{\pi}^c, V_v^c; \lambda_{\pi}^{so}, \lambda_v^{so}\}, \quad (14)$$

but the two sets can be seen as playing equivalent roles in the functioning of the phenomenological Hamiltonian.

The Schrödinger equation with our mean-field Hamiltonian is solved by using standard diagonalization methods employing the matrix representation of the Hamiltonian within the anisotropic harmonic-oscillator (HO) basis. The HO basis cutoff conditions have been adjusted to assure that the calculated bound single nucleon energies remain stable within three decimal places at the extremes of the zones of variations of the deformation parameters; see Ref. [44] for details.

### C. Impact of the parameter adjustment on stability and uncertainties of predictions

The parameter adjustment algorithms employ experimental data, each datum characterized by an error-bar expressing the datum's uncertainty. The existence of these uncertainties implies that the resulting optimized parameters are themselves uncertain and should be presented together with their uncertainty probability distributions. With this information one can estimate in particular the final modeling uncertainties of predicted observables of interest. It then follows that contemporary parameter adjustment algorithms, like, e.g.,  $\chi^2$  tests used to provide the optimal fit solutions represent merely the beginning of a longer chain of steps bringing in prediction uncertainties. Let us note that leading international journals strongly encourage verification of the modeling uncertainties before publishing the corresponding predictions, cf., e.g., the Physical Review Editorial in Ref. [52].

One of the first, most direct recommendations imposed by the inverse problem theory of applied mathematics is the verification that the parameters resulting from the adjustment procedure are free from parametric correlations. This requirement is fundamental since one may demonstrate rigorously that modeling with parametric correlations implies an asymptotically vanishing predictive power for the data outside of the fitting zone, cf., e.g., Secs. III and IV of Ref. [44] and references therein. Occasionally one may be talking about an exponential divergence of predictions from the results which could be expected in case of stable solutions in such a case.

Parametrization of the Hamiltonian used in the present project has been optimized by employing the well-established methods of the inverse problem theory. We have used among others the Monte Carlo simulations with the help of which the presence of nonlinear parametric correlations has been determined. These correlations have been consecutively eliminated. Not entering into details at this point let us mention

TABLE I. Parameters of the universal Woods-Saxon Hamiltonian from Ref. [44]; upper row—protons, lower row—neutrons. The dependent parameters resulting from the procedure of elimination of the parametric correlations are  $r_{\pi}^c = 1.278$  fm,  $r_v^c = 1.265$  fm,  $r_{\pi}^{so} = 0.830$  fm,  $r_v^{so} = 0.890$  fm. The spin-orbit diffusivity parameters are  $a_{\pi}^{so} = a_v^{so} = 0.700$  fm, see Ref. [44].

	$V_0^c$ (MeV)	$\kappa^c$	$a_{\pi,v}^c$ (fm)	$\lambda_0^{so}$	$\kappa^{so}$
Mean values	-50.225	0.624	0.594 0.572	26.210	-0.683
Standard error	0.142	0.013	0.010 0.011	0.513	0.139

that 4 among 12 original Woods-Saxon potential parameters were found correlated. After eliminating the correlations, the final set contains only eight independent parameters. The interested reader can find the details in Ref. [44], whereas the numerical values of the concerned parameters are given in Table I.

It will be instructive to illustrate at this point the predicted single nucleon spectra and the spherical shell structures together with the corresponding energy gaps. The results characteristic for the nuclei in the  $Z/N$  range covered in this article are shown in Fig. 1.

The proton spherical shell gap of the order of 2 MeV at  $Z = 114$  is visible from the single-particle energy diagram, Fig. 1, top. Its size expresses directly the repulsive spin-orbit interaction between the  $2f_{7/2}$  and  $2f_{5/2}$  orbitals. In the case of the neutrons, the spherical shell gaps at  $N = 164, 184, 228,$  and  $258$  deserve noticing—compare with early predictions in Ref. [53].

Spherical shell gaps at  $Z = 114$  and  $N = 184$  were predicted in several publications using various theory frameworks, cf. Refs. [23,26,28]. More precisely, the spherical neutron shell-gap sequence  $N = 126, 164, 184, 228,$  and  $258$  was discussed as early as in Ref. [53] based on even earlier Woods-Saxon potential parametrizations, Refs. [55–57], evidently a robust feature of this potential since reproduced also in this project using very different parameter optimization arguments. Some of those shell closures appear modeling dependent, such as, e.g.,  $N = 228$ , cf. Refs. [31,58,59]—alternatively the corresponding  $N = 228$  nuclei can be predicted to be nonspherical.

Figures 2 and 3 complete the information about the single-particle levels illustrated in Fig. 1, now showing the uncertainty distributions of the nucleonic energies obtained with the optimized Hamiltonian—representative for the mean-field description employed in this project. The widths of probability distributions of energy-level uncertainties turn out to vary with nucleonic orbital angular momentum quantum number  $\ell$ . They increase on average with increasing orbital angular momentum, even though the increase undergoes certain fluctuations. To give the orders of magnitude of the discussed variation, the full width at half maximum (FWHM) for neutron energies is approximately 0.24 MeV for the  $1s_{1/2}$  level and about 0.43 MeV for the  $1k_{17/2}$  level.

The characteristics of the proton levels are similar.

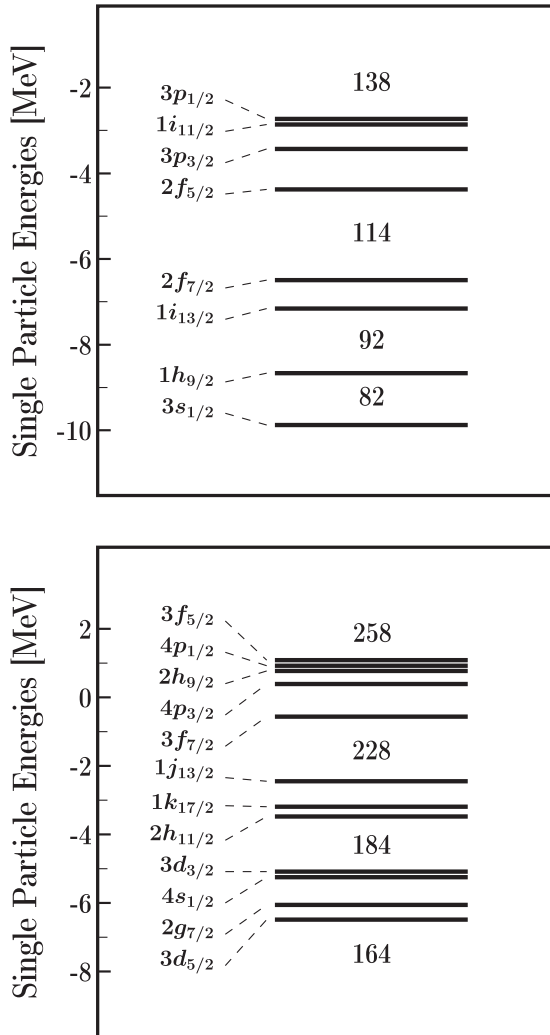


FIG. 1. Single-particle proton (top) and neutron (bottom) energies showing the spherical orbital energies and the accompanying strongest spherical shell gaps. These results were obtained with the newly adjusted parameters using the spherical doubly magic nuclei which can be considered relatively far from the mass zone of interest here; parametric correlations were detected and removed, cf. Ref. [44]. The appearance of the  $N = 196$  universal magic gap turns out to result from the octupole repulsion between the  $\Delta\ell = 3$  neutron orbitals  $2h_{11/2}$  and  $1k_{17/2}$  visible above the spherical gap  $N_{\text{sph}} = 184$ , cf., the arguments we present qualitatively in the vicinity of Eq. (2); It follows that  $184 + (2j + 1)|_{j=11/2} = 184 + 12 \rightarrow N = 196$ .

### III. TETRAHEDRAL SYMMETRY AND OTHER OCTUPOLE-TYPE SHELL EFFECTS ON STABILITY OF SUPERHEAVY NUCLEI

We now address the issues of the symmetry-induced increase in stability of the discussed superheavy nuclei. Such an increase takes place when the energy minima are getting lower (increasing binding) and the separating potential barriers get higher (generally weakening the corresponding decay modes). To examine these effects we employ the realistic phenomenological nuclear mean-field theory techniques introduced earlier, combined with the geometrical symmetry

considerations, which involve application of the molecular point group concepts.

Let us begin with the tetrahedral symmetry effects generated by the so-called “tetrahedral-octupole” ( $\alpha_{32}$ ) deformation, below also referred to as “tetrahedral” for short. This symmetry should be given all our attention since it is clearly a dominating one. We will address separately alternative point-group symmetries  $C_{2v}$ ,  $D_{2d}$ , and  $D_{3h}$  generated, respectively, by  $\alpha_{31}$  alone or a combination of  $\alpha_{31}$  and  $\alpha_{20}$ , by combination of  $\alpha_{32}$  and  $\alpha_{20}$  and by  $\alpha_{33}$  alone or a combination of  $\alpha_{33}$  and  $\alpha_{20}$ .

Before discussing the properties of the nuclear potential-energy surfaces generated by the presence of the point-group symmetries and the nuclei in which the discussed mechanisms are the strongest, it will be instructive to illustrate the octupole shell effects and the underlying single-nucleon energy gaps. With this goal in mind, in the next section we will compare the diagrams of the proton and neutron single-particle energies as functions of the four octupole deformations:  $\alpha_{30}$ ,  $\alpha_{31}$ ,  $\alpha_{32}$ , and  $\alpha_{33}$ .

#### A. Single-particle spectra generated by pure octupole deformations: Octupole shell effects

Proton single-particle energy spectra generated by the four octupole deformations are presented in Fig. 4, where all other deformations are set equal to zero. The strongest proton shell gaps appear at  $\alpha_{32}$  tetrahedral deformation. They are manifested by single-gap patterns for  $Z = 106$ , 116, 124, and 136. Otherwise, the octupole proton shell effects “measured by gaps” do not appear strong from reading single-particle diagrams except for the low level-density zones in the vicinity of  $Z = 124$ . Generally, for heavy nuclei with relatively densely distributed single-particle energies, the analysis by reading single-particle energy diagrams is often inconclusive or misleading so that the effective comparison of various zones can only be accomplished by presenting calculated nuclear shell energies, which will be done next.

Analogous single-particle energy spectra for neutrons are shown in Fig. 5. The strong shell effects manifested by a strong-gap pattern are seen only for the tetrahedral-symmetry deformation at  $N = 196$ , an effect accompanied by a smaller, secondary gap at  $N = 202$ .

Let us emphasize that the size of the  $N = 196$  tetrahedral gap is comparable with the size of the spherical gap at  $N = 184$ , both gaps corresponding to about 2 MeV spacing. However, as indicated by all four diagrams, our calculations also predict octupole effects in the form of the low-density pattern of single-particle levels for other octupole deformations—placed in the vicinity of the same  $N = 196$  particle-number zone. Under these circumstances there is only one way of accomplishing the analysis of the effective octupole shell effects in the studied case: by effectively calculating and comparing the Strutinsky shell energies. This will be discussed more systematically later in the following sections.

The specificity of the tetrahedral symmetry consists in the fact that the underlying tetrahedral double point group  $T_d^D$ , the tetrahedral-symmetry group of the mean-field fermion Hamiltonian, is one of the most exotic in the family of molecular

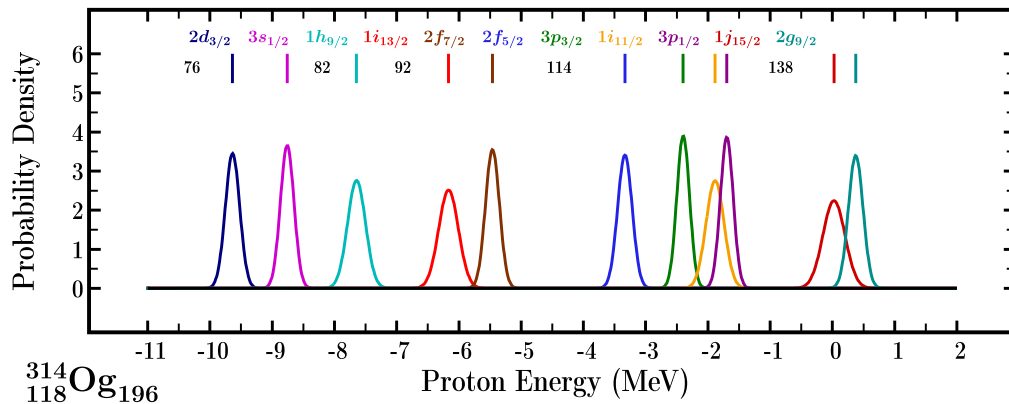


FIG. 2. Monte Carlo simulated probability distributions of single-particle level position uncertainties for protons in the  $^{314}\text{Og}$  nucleus; selected levels surround the  $Z = 114$  gap. The vertical bars accompanied by the spectroscopic labels show the positions of the corresponding peaks of the distributions; for details cf. Ref. [54].

(point-group) symmetries. It contains 48 symmetry elements and among its three irreducible representations there are two two-dimensional and one four-dimensional, the latter thus inducing the fourfold degenerate single nucleon energies. It has been argued in our earlier articles that these special properties contribute to lowering, on average, the single-particle level densities leading occasionally to particularly strong gap openings and strong shell-effects (low level density zones) as indeed manifested in the illustrated spectra.

As is visible from Fig. 1, bottom, the neutron spacing at  $N = 196$  (attention, the corresponding gap is not strongly visible *at spherical shape* and is not marked with the occupation label) separates the sequence of “lower-lying orbitals” ending at  $2h_{11/2}$  from the sequence of “higher-lying orbitals” beginning with  $1k_{17/2}$ . The fact that the octupole shell effects around the neutron number  $N = 196$  occur at all four octupole deformations can be attributed to the repulsion by the residual octupole-octupole interaction between the orbitals  $1k_{17/2}$  from the  $\mathcal{N} = 8$  shell and  $2h_{11/2}$  from the  $\mathcal{N} = 7$  shell ( $\Delta\ell = \Delta j = 3$ )—according to spectroscopic labeling in Fig. 1.

In fact there are more orbitals characterized by the  $\Delta\ell = \Delta j = 3$  condition, which contribute to the repulsion at  $N = 196$ , caused by the residual octupole-octupole interaction

Hamiltonian proportional to  $\hat{Q}_3^\dagger \otimes \hat{Q}_3$  interaction term (alternatively octupole-deformed mean-field potential); these orbitals are listed in Table II.

Let us recall that the relation between the pairs of interacting or repelling orbitals together with the generated gap-openings and induced shell structures as function of the preselected multipolarity  $\lambda$  has been discussed in detail in Ref. [60] in relation to the multipole-multipole residual interaction Hamiltonians (alternatively, the mean field deformed ones). Analytical expressions addressing the mechanism of repulsion between the  $\Delta\ell = 3$  orbitals leading to possibly strong shell gaps when increasing the octupole deformations can be found in Appendix C of the above reference, cf. in particular Eq. (C1).

### B. Characteristic behavior of potential energies in the vicinity of $N = 196$ octupole gap

Potential-energy surfaces within  $\{\alpha_{20}\text{-vs-}\alpha_{3\mu=0,1,2,3}\}$  representation are illustrated after minimization over  $\alpha_{40}$  for the  $^{310}\text{Fl}_{196}$  nucleus in Fig. 6. A comparison shows that all the double minima at  $\alpha_{3\mu} \approx 0.15$  correspond to the vanishing quadrupole deformation  $\alpha_{20} = 0$ , similarly to the case of  $^{218}\text{Pb}_{136}$ , cf. Fig. 6 of Ref. [3]. These results indicate that the

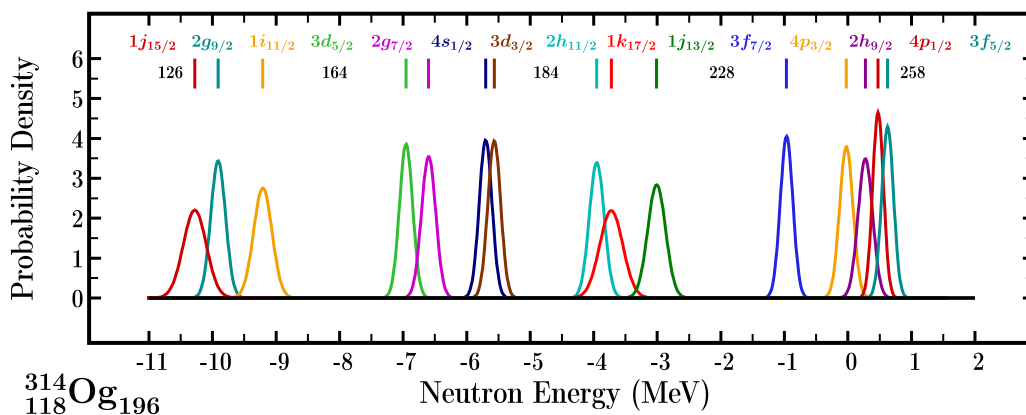


FIG. 3. Illustration similar to the preceding one but for the neutron levels surrounding the  $N = 184$  gap.

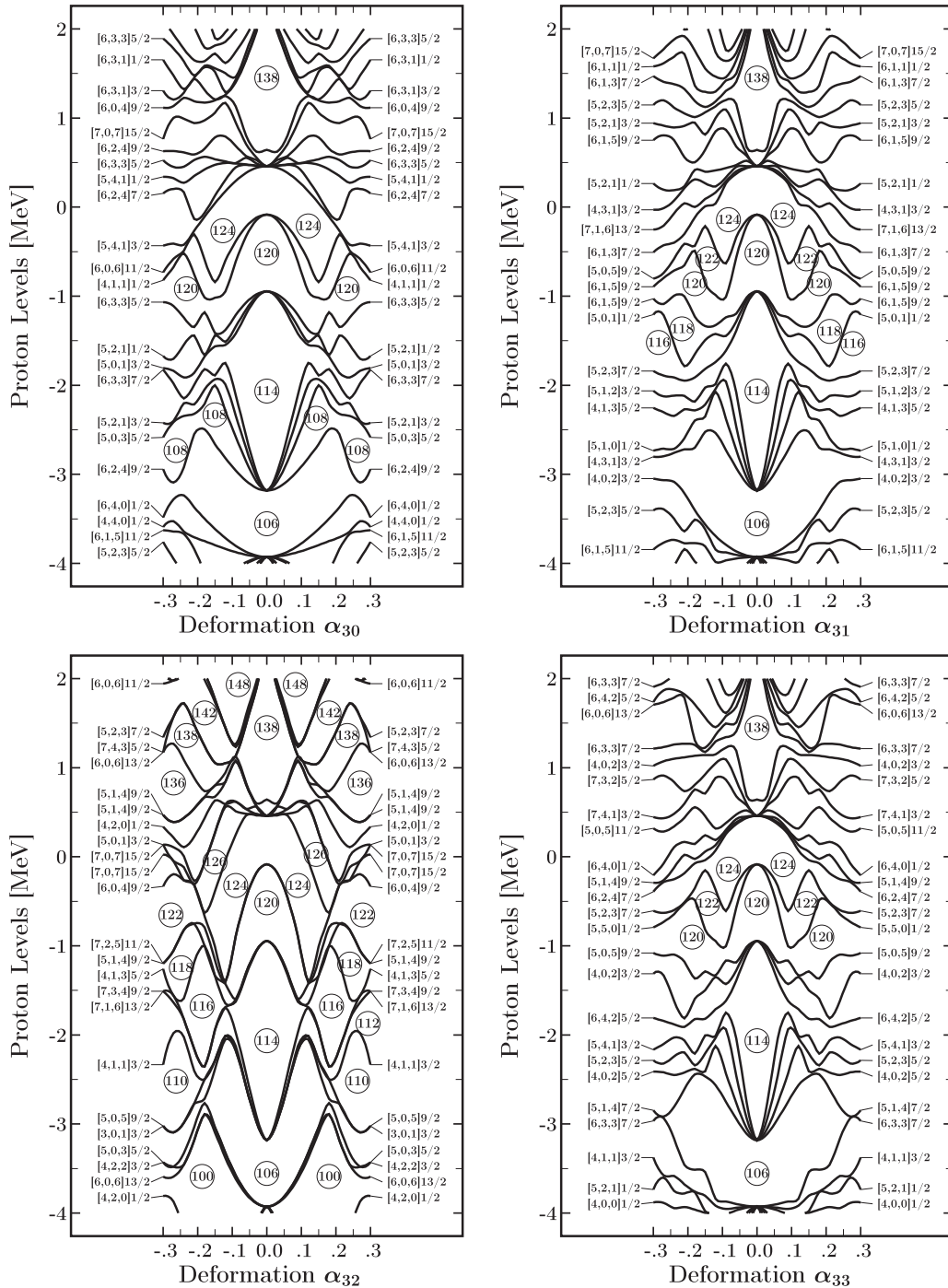


FIG. 4. Proton single-particle energies as functions of the octupole deformations  $\alpha_{3\mu=0,1,2,3}$  predicted for the superheavy nuclei discussed in this article. The central nucleus is chosen to correspond to the center of the  $(Z, N)$ -zone addressed in this article:  $Z_0 = 122$  and  $N_0 = 186 \leftrightarrow (114 \leq Z \leq 130$  and  $166 \leq N \leq 206)$ . It has been verified by direct calculations that no characteristic features illustrated depend significantly on this choice. All other deformation parameters are set to zero. In the case of  $\alpha_{32}$  deformation, the results indicate the presence of “narrow vertical gaps” at  $Z = 106, 116,$  and  $124$ , whereas for all other deformations there are no strong octupole shell effects visible, except for  $Z = 106$  spacing. Let us emphasize the unusual, original property of the  $\alpha_{32}$ -type diagrams: some curves are labeled with two Nilsson labels. This happens where the level belongs to a four-dimensional irreducible representations of the double tetrahedral point group  $T_d^D$ , as discussed in the text.

neutron magic number  $N = 196$  has indeed all the features of the universal fourfold octupole magic number introduced in the cited article.

The highest barrier separating the octupole twin minima visible from the plot corresponds to the tetrahedral deformation, with the barrier heights of the order of 3 to 4 MeV. The

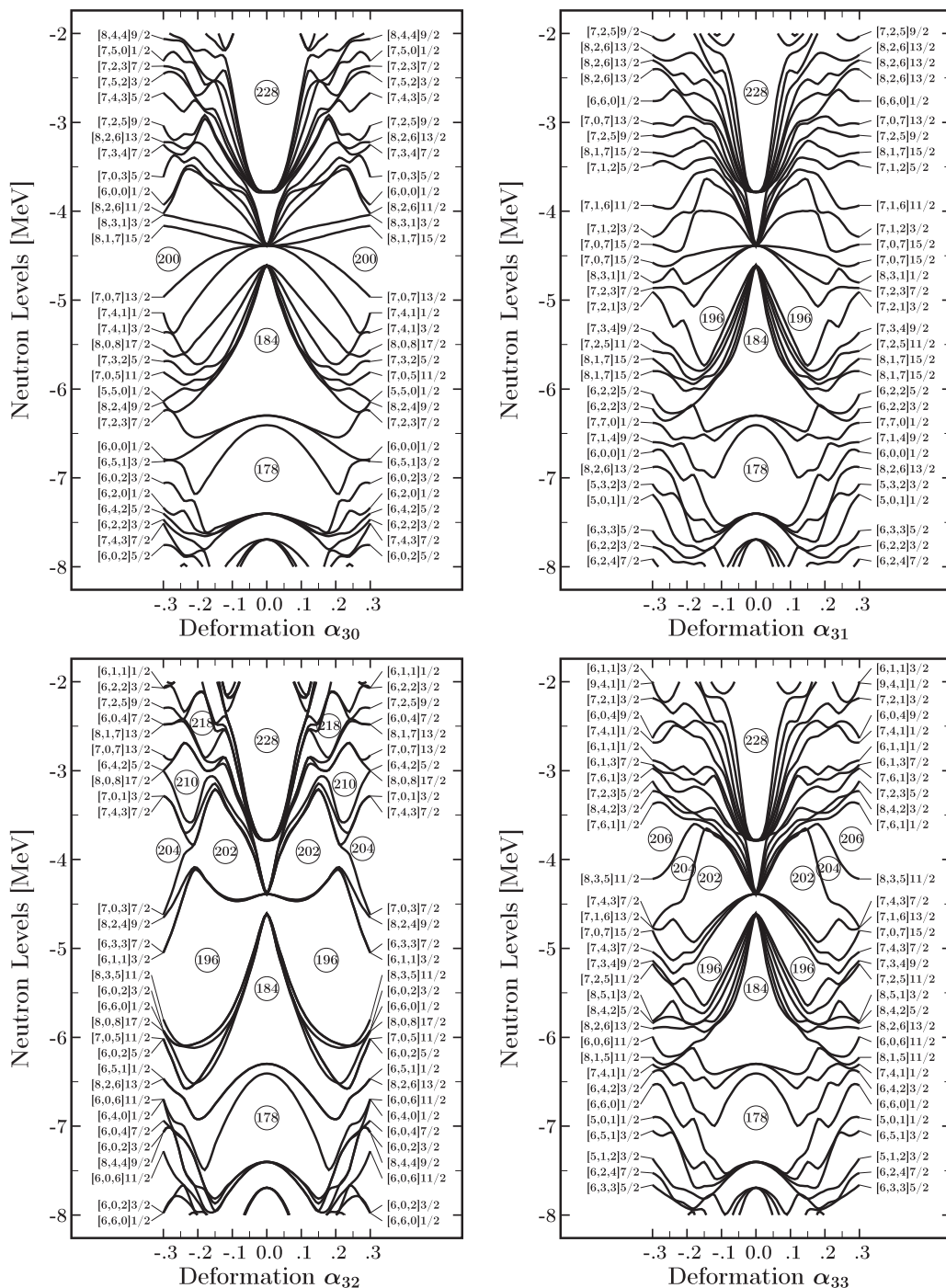


FIG. 5. Neutron single-particle energies as functions of the octupole deformations  $\alpha_{3\mu=0,1,2,3}$  predicted for the superheavy nuclei studied in this article. All other deformation parameters are set to zero, central nucleus  $Z_0 = 122$  and  $N_0 = 186$ . The strongest octupole shell effect is visible at  $N = 196$ , caused by the tetrahedral-symmetry  $\alpha_{32}$  deformation, but the area of low density of single-particle energies—which directly influences Strutinsky shell energies—extends between  $N = 196$  and 202. Similarly, low-density zones (without strong gaps *sensu stricto* at  $N = 196$ ) are visible also for the deformations  $\alpha_{30}$ ,  $\alpha_{31}$ , and  $\alpha_{33}$ , where the  $N = 196$  area is clearly accompanied by the low level densities. We emphasize that, as in the case of the proton  $\alpha_{32}$ -diagrams, certain orbitals are identified with the double Nilsson labels, i.e., those belonging to the four-dimensional irreducible representations of the double tetrahedral point group  $T_d^D$ . It is this latter property which greatly contributes to the strong shell effects generated by tetrahedral symmetry, as discussed in the text and in the earlier publications by our collaboration.

TABLE II. Orbitals with  $\Delta\ell = \Delta j = 3$ , which are found in the single-particle spectrum on the opposite sides of the  $N = 196$  separation and thus contribute to an increase of the corresponding gap size with increasing  $\alpha_{3\mu}$ .

$\Delta\ell = \Delta j = 3$
$1k_{17/2} \leftrightarrow 2h_{11/2}$
$1j_{13/2} \leftrightarrow 2g_{7/2}$
$3f_{7/2} \leftrightarrow 4s_{1/2}$
$2h_{9/2} \leftrightarrow 3d_{3/2}$

fission barrier in the case of the  $(\alpha_{32}$ -vs- $\alpha_{20})$  plane reaches the energy order of 3 to 4 MeV as well. In contrast with tetrahedral deformation, the remaining octupole components, i.e.,  $\alpha_{30}$ ,  $\alpha_{31}$ , and  $\alpha_{33}$ , produce the relatively low fission barrier heights of the order of 1.5 to 2 MeV.

Since, as shown in the preceding illustration, tetrahedral deformation manifests the strongest shell effects, which lead to lowering the nuclear potential energies most significantly and generating the most pronounced shape competition effects, it will be instructive to examine the evolution of these effects at the expected strongest tetrahedral-bound neutron configuration  $N = 196$  for varying proton number. The corresponding sequence of potential-energy maps for  $Z = 118$ , 122, 126, and 130 is illustrated in Fig. 7. Two tendencies can be observed.

First, a very characteristic strong increase of the barriers separating the two tetrahedral minima, beginning with 5.5 MeV for  $Z = 118$  and continuing with 8 MeV at  $Z = 122$  up to the huge, probably the highest so far calculated in nuclear structure, 10 MeV at  $Z = 126$  and about 12 MeV at  $Z = 130$ .

Second, an increase in proton number from  $Z = 118$  to 130 is accompanied by lowering the energy of the competing, axially symmetric quadrupole minimum at  $\alpha_{20} \approx -0.28$ , together with the simultaneous increase in the barriers between those and tetrahedral twin-minima.

The comparisons presented in Figs. 6 and 7 can be seen as showing extreme (the strongest) form of manifestation of the tetrahedral symmetry effects and their impact on an increase in stability of superheavy nuclei in the studied region. In many surrounding nuclei similar types of dependencies apply, even though the extreme energy variations visible here are getting less and less pronounced.

### C. Shell energies as functions of octupole deformations

As noticed earlier, for nuclei with big numbers of nucleons and relatively closely spaced single-particle energies, it is in general difficult to deduce the information about quantum shell closures by reading single-particle spectra. It will therefore be instructive to present the related numerical results for the shell energies directly as obtained from the Strutinsky approach.

Figure 8 shows the nuclear shell energies, composed of Strutinsky and BCS pairing correlation energies, as functions of octupole deformations  $\alpha_{30}$ ,  $\alpha_{31}$ ,  $\alpha_{32}$ , and  $\alpha_{33}$ , for nuclei with  $Z = 114$  and neutron numbers varying between  $N = 190$

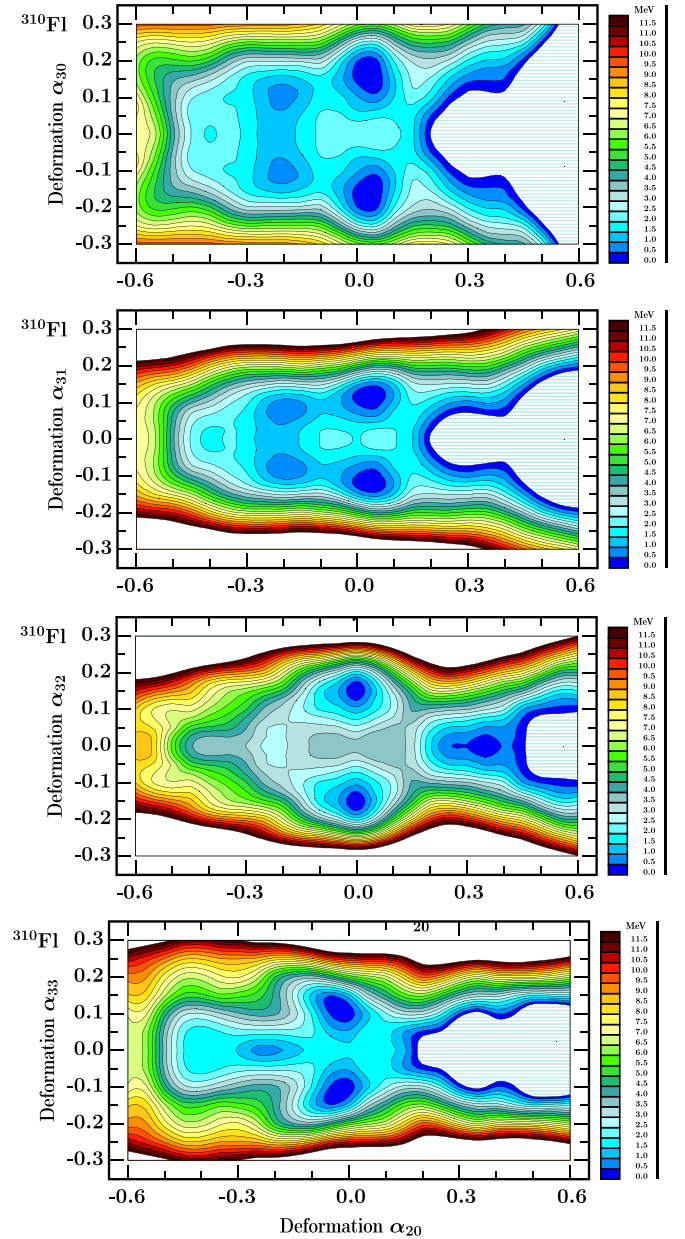


FIG. 6. Projections of the total energy on  $(\alpha_{20}, \alpha_{3\mu=0,1,2,3})$  planes, contour-line separation of 0.5 MeV, minimized at each deformation point over axial hexadecapole deformation  $\alpha_{40}$ , for the  ${}^{310}_{114}\text{Fl}_{196}$  nucleus. Let us notice that, for  $\mu \neq 2$ , the octupole deformed double minima are accompanied by relatively low fission barriers and are thus less fission-stable (fission barriers of the order of 2 MeV) whereas for the tetrahedral symmetry minima the fission barriers are of the order of 3 to 4 MeV.

and  $N = 210$ . The presence of the octupole energy minima in all four octupole deformation components at  $\alpha_{3\mu} \approx \pm 0.2$  confirms the presence of the underlying low-level-density zones in the studied superheavy nuclei, deduced qualitatively from Figs. 4 and 5.

Figure 9 contains similar illustrations for the shell-energies with varying proton number at the fixed neutron number,  $N = 196$ . The close-lying curves corresponding to the varying

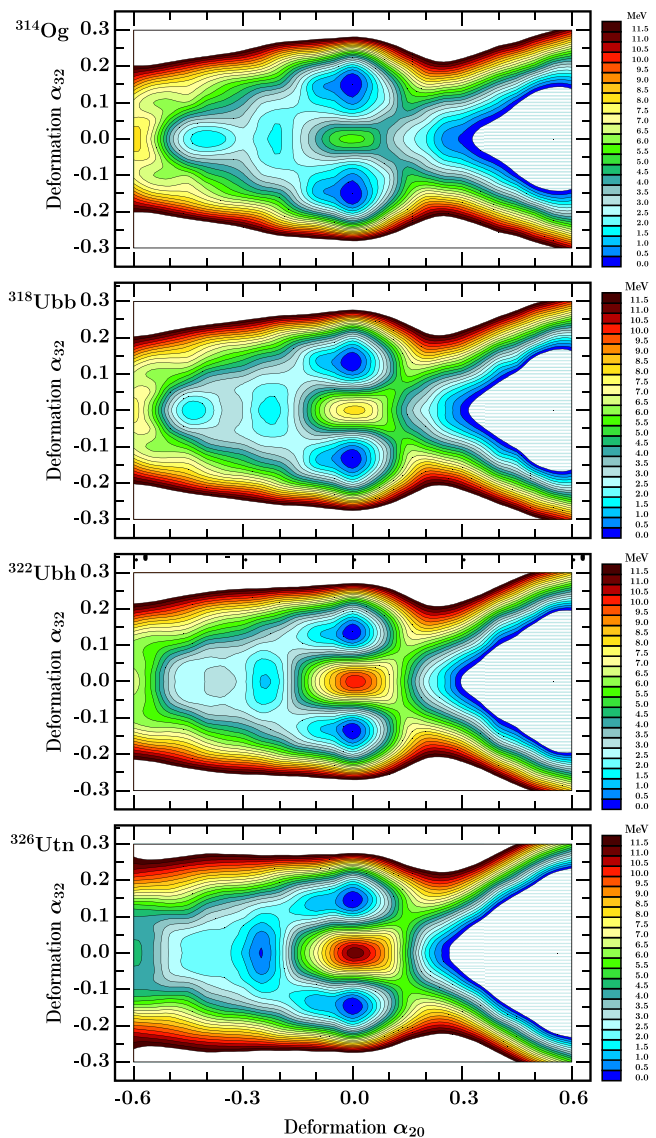


FIG. 7. Selected potential-energy projections with contour-line separations of 0.5 MeV. They present octupole-tetrahedral shape evolution at  $N = 196$  for oganesson, unbibium, unbihexium, and untrinitium, thus with proton numbers  $Z = 118, 122, 126, 130$ , respectively. The two symmetric tetrahedral (twin) quadrupole deformation  $\alpha_{20} = 0$  are very well developed. They are separated by the potential barriers of up to 10 MeV. The fission barrier heights increase with increasing proton number.

proton number signify that the structure of the octupole dependence of the studied quantities is mainly due to the neutrons. The proton effects on the variation of the shell-energy minima are restricted to a couple of hundred keV.

Observing the average energy positions of the shell-energy minimum values and comparing with one another in each of the four diagrams in Fig. 9 (they are centered approximately, at the level of  $-4$  MeV for the  $\alpha_{30}$  and  $\alpha_{31}$  cases, at  $-3$  MeV for  $\alpha_{33}$ , as compared with  $-9$  MeV for  $\alpha_{32}$ ) we may conclude that the tetrahedral symmetry again wins significantly the competition among all four octupole deformation effects.

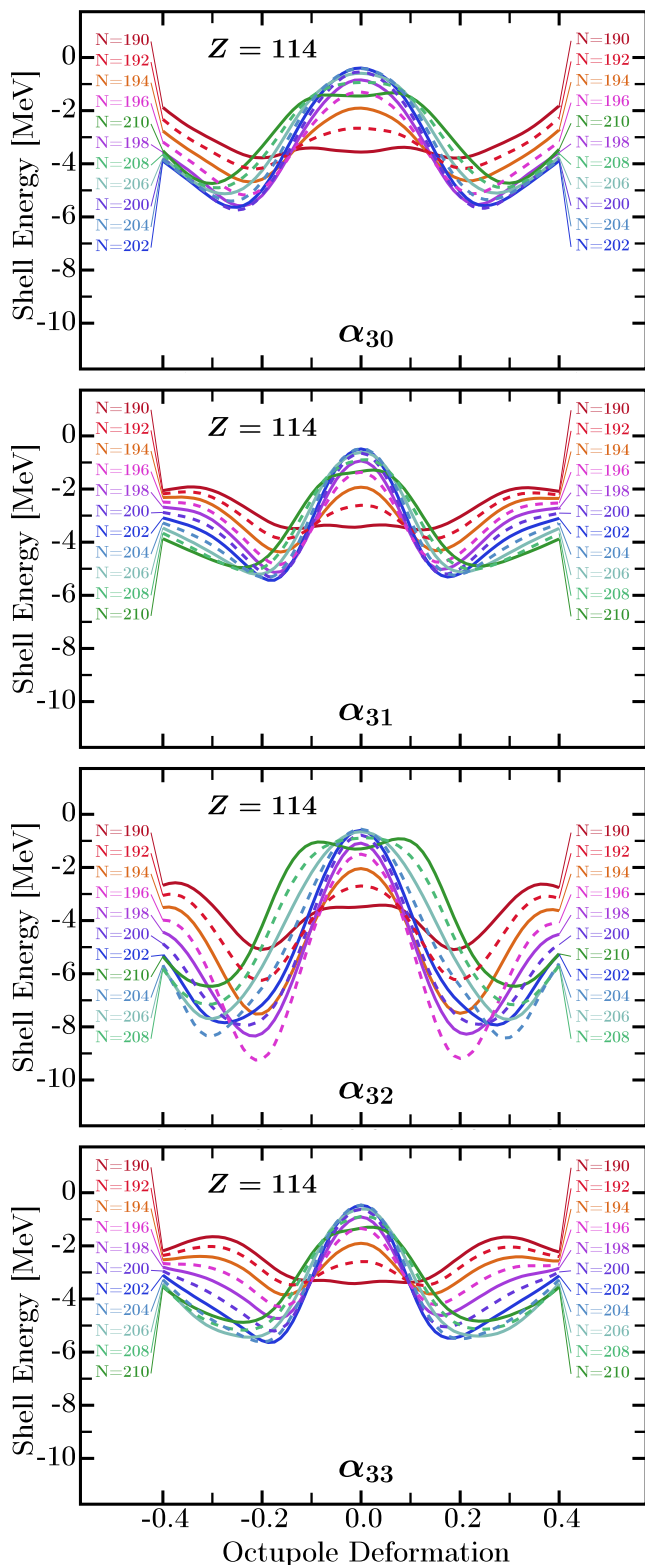


FIG. 8. Nuclear shell energies as functions of octupole deformations  $\alpha_{3\mu=0,1,2,3}$  for  $Z = 114$  and neutron numbers between  $N = 190$  and  $N = 210$ . The strongest shell effects show up in the case of  $\alpha_{32}$  deformation (tetrahedral symmetry) dominated by  $N = 196$ .

The discussed global (repetitive) behavior of the results in the two diagrams confirms the usefulness of both the concept

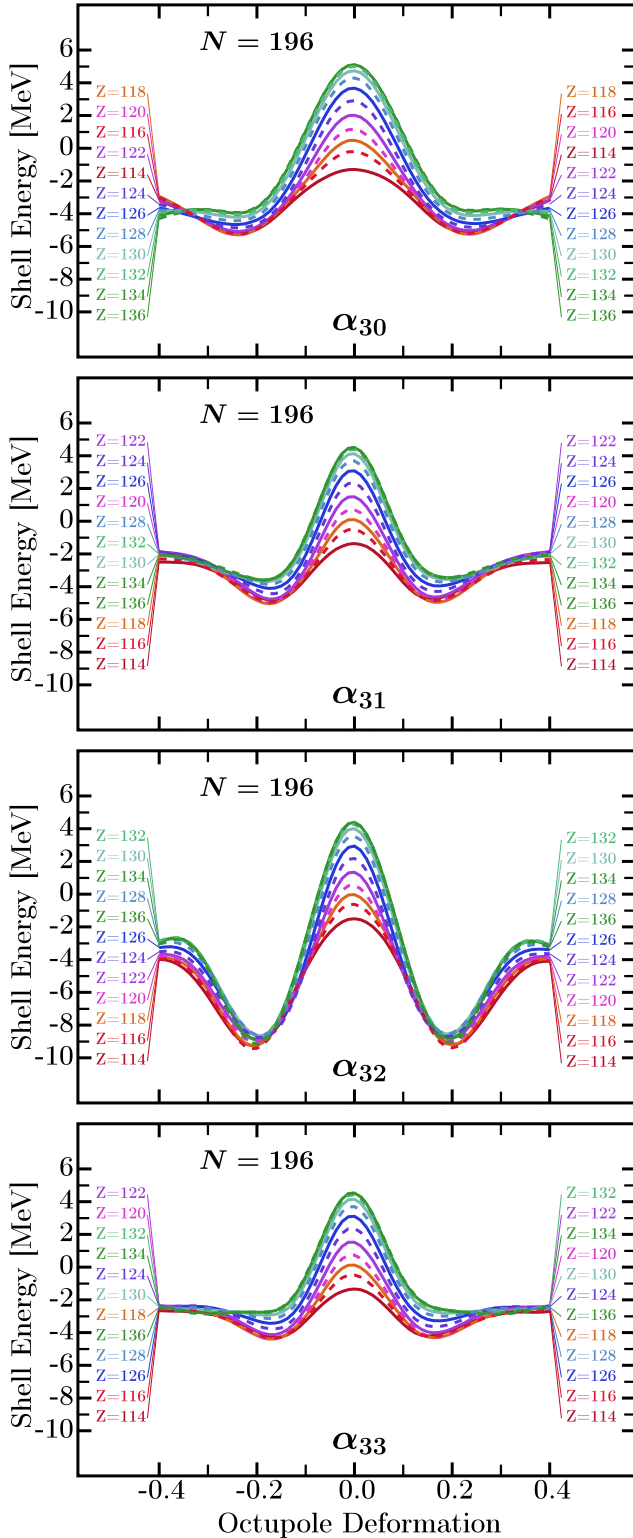


FIG. 9. Illustration similar to that in Fig. 8, but for the neutron number  $N = 196$  with varying proton numbers from  $Z = 114$  to  $Z = 136$ . Once again, the most pronounced nuclear shell effects appear for tetrahedral- $\alpha_{32}$  deformation for all nuclei.

and terminology behind the universal (or fourfold) octupole magic number. This magic number can be seen as the name

TABLE III. Energies at the equilibrium before allowing the  $\alpha_{32}$  minimization, column five, compared with the equilibrium energies when allowing the minimization over  $\alpha_{32}$ , column four, and the deformation at the minimum, column three. Differences between the two energy minima with  $\alpha_{32} \neq 0$  and  $\alpha_{32} = 0$ , column six. Results correspond to nuclei with proton number  $Z = 106$  and neutron numbers varying between  $N = 190$  and  $N = 210$ . Energies are in MeV.

$Z$	$N$	$\alpha_{32}^{\min}$	$E_{\min}^{\alpha_{32} \neq 0}$	$E_{\min}^{\alpha_{32} = 0}$	$\Delta E_{\min}$
106	190	0.10	-3.017	1.013	4.030
106	192	0.11	-3.308	2.041	5.349
106	194	0.13	-3.682	2.926	6.609
106	196	0.15	-4.418	3.658	8.076
106	198	0.13	-3.554	4.236	7.790
106	200	0.12	-2.937	4.654	7.591
106	202	0.12	-2.253	4.913	7.166
106	204	0.12	-1.445	5.010	6.455
106	206	0.11	-0.565	4.952	5.516
106	208	0.11	0.257	4.736	4.479
106	210	0.10	0.981	4.368	3.387

of the mechanism manifesting very strong energy-stabilizing quantum relation impacting literally dozens of even-even nuclei directly illustrated in our diagrams. One should be aware that the even-even nuclei very often predetermine the shape properties of the neighboring even-odd and odd-even neighbors, which triples the number of affected cases. Including the odd-odd nuclei, whose energy vs deformation effects are to far extent predetermined by the same neighboring even-even ones, we are going to increase the number of cases for the second time. We may conclude that the two discussed diagrams with a few dozen curves contribute to a synthetic message about octupole instability in several hundreds of superheavy nuclei in the studied zone.

Analogous conclusions can be drawn out of the comparison of the total potential-energy diagrams, which will be presented in the following section.

Before completing the overview, it may be instructive to compare energies gained by each nucleus when allowing energy minimization over  $\alpha_{32}$ . The corresponding results are shown in Tables III and IV for series of isotopes related to  $Z = 106$  and  $Z = 124$ , respectively.

#### D. Comparison of nuclear potential energies: Universal fourfold octupole magic number

Arriving at this point of the discussion we know already that the leading role in generating the four-dimensional octupole-type shape-driving effects as well as the associated relative mass stabilization in the discussed superheavy nuclei is played by the  $N = 196$  fourfold octupole magic gap. Thus, as before, we construct the illustrations in such a way that the leading element ( $N = 196$  configuration) remains in the center of the diagram, which will be filled in with the curves for the neighboring  $N$  values. In this way we will be able to accentuate possible similarities of behavior associated with the neutron shell structures, since in such a selection the

TABLE IV. Similar to Table III, but for nuclei with proton number  $Z = 124$ .

$Z$	$N$	$\alpha_{32}$	$E_{\min}^{\alpha_{32} \neq 0}$	$E_{\min}^{\alpha_{32} = 0}$	$\Delta E_{\min}$
124	190	0.11	-2.363	1.127	3.490
124	192	0.12	-2.650	2.147	4.797
124	194	0.13	-3.030	3.004	6.034
124	196	0.15	-4.413	3.685	8.098
124	198	0.14	-3.509	4.187	7.696
124	200	0.14	-3.012	4.505	7.517
124	202	0.14	-2.458	4.637	7.096
124	204	0.13	-1.662	4.586	6.248
124	206	0.13	-0.876	4.347	5.224
124	208	0.12	-0.155	3.926	4.081
124	210	0.10	0.478	3.338	2.861

proton shell effects will be, to leading order, nearly equal for each family of isotopes.

Since the strongest proton octupole shape effects are predicted to be centered at  $Z = 106$  and  $Z = 124$ , cf. Fig. 4, we collect the corresponding curves for  $Z = 106$  nuclei in Fig. 10 presenting the dependencies in terms of  $\alpha_{30}$ ,  $\alpha_{31}$ ,  $\alpha_{32}$ , and  $\alpha_{33}$  in separate diagrams. In analogy, Fig. 11 collects the results for the  $Z = 124$  isotopes.

Let us suggest, as the first step of the proposed comparative analysis, observing analogies between the left-hand side and the right-hand side partner diagrams in each series. This comparison is facilitated by the graphical display rules attributing to the same isotone the same typographical characteristics: the compared curves are either marked both as dashed or full lines, and both in the same color. Indeed, the similarities are far-reaching.

One can directly observe pronounced analogies between the two groups of isotopes despite the fact that the proton numbers differ by nearly 20 charge units. In particular, the minimum energies of compared curves in the case of tetrahedral deformation are spread in about 5 MeV energy intervals in both groups. In the case of the pear-shape deformations the corresponding spreading interval is about 3 MeV for  $Z = 106$  and about 2 MeV for  $Z = 124$ . At the same time, the spreading in question amounts to 2 MeV for  $Z = 106$  and about 1.5 MeV for  $Z = 124$  in the case of  $\alpha_{31}$  and  $\alpha_{33}$ .

It is neither our intention nor the place in this article to review the rich literature of the systematic predictions of equilibrium deformations or other predicted properties of superheavy nuclei published so far by other authors. Nevertheless, we believe that a limited overview focused specifically on the predictions related to the octupole shapes and related symmetry effects will be instructive. Among the four octupole-deformation components, the one with axial symmetry, i.e., the “pear-shaped” deformation, was receiving by far more attention than the others.

In particular, pear-shape deformations for  $Z = 106$  and  $N = 194$  to 200 nuclei were predicted in Ref. [5] following the calculations with the NL3\* type covariant energy density-functional mean-field formulation. The predictions of the octupole- $\alpha_{30}$  deformation in the region of  $Z \approx 100$  and

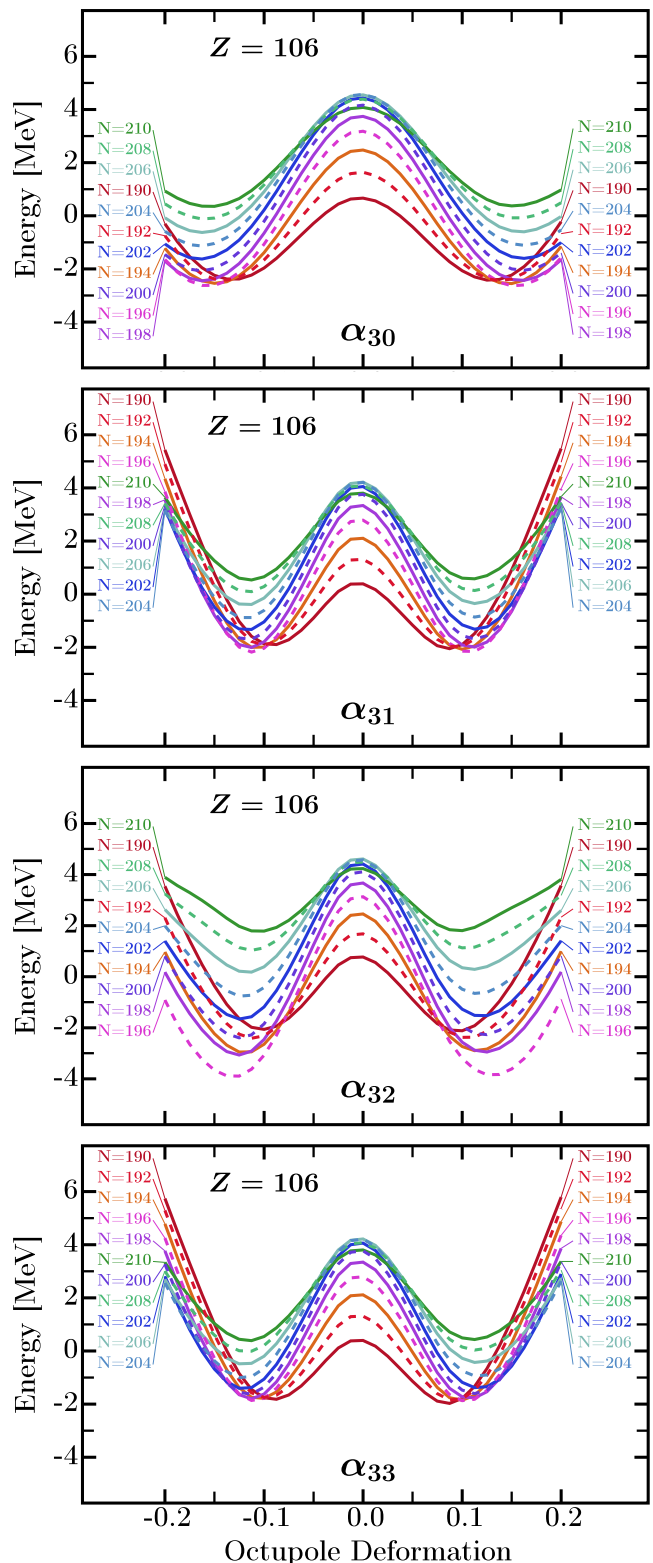


FIG. 10. Illustration of nuclear potential energies as functions of octupole deformations for nuclei with the proton number  $Z = 106$  with varying neutron numbers from  $N = 190$  to  $N = 210$ . The strongest nuclear deformation-driving effects appear for the tetrahedral- $\alpha_{32}$  deformation for all nuclei. Normalization is specified by setting the macroscopic energy equal to zero at vanishing deformation.

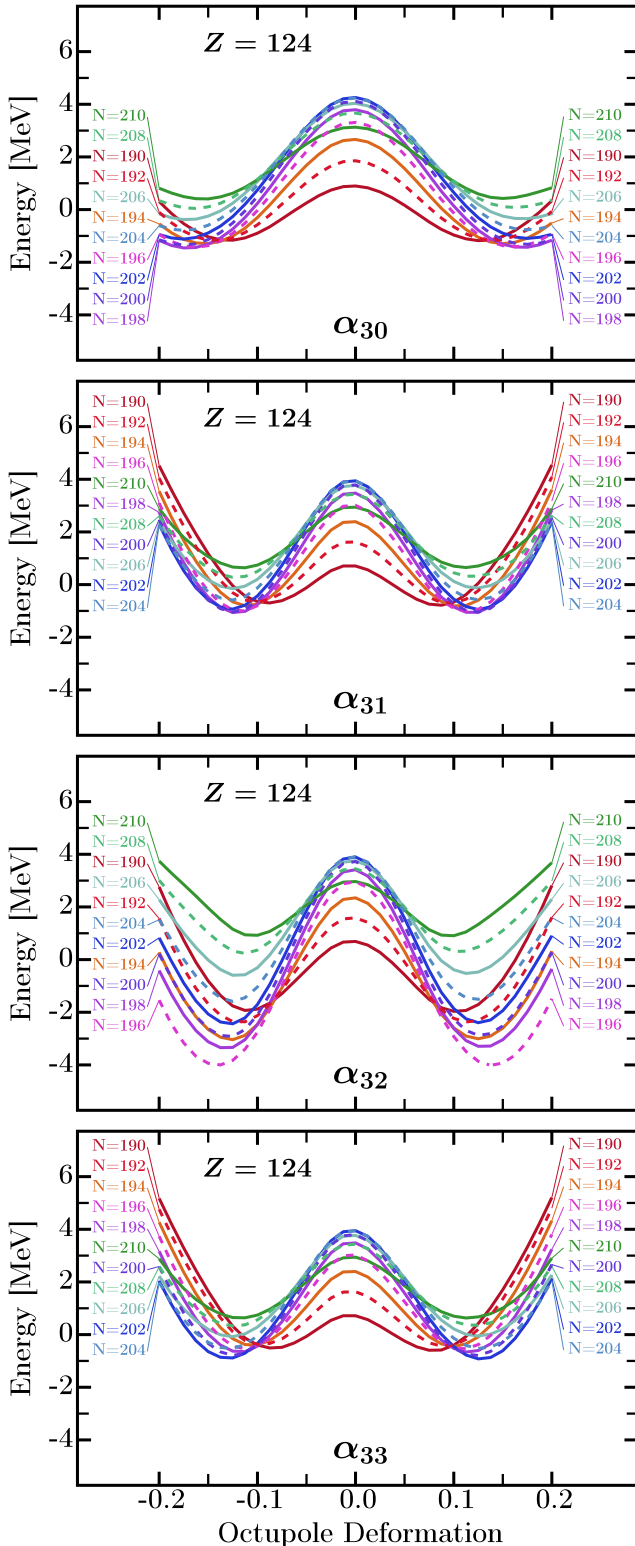


FIG. 11. Illustration similar to that in Fig. 10, but for the proton number  $Z = 124$  with varying neutron numbers from  $N = 190$  to  $N = 210$ . As in the preceding case, the most pronounced nuclear shell effects appear for the tetrahedral- $\alpha_{32}$  deformation for all nuclei. For normalization of the curves, see caption to Fig. 10.

$N \approx 196$  using various theoretical methods are collected in Fig. 7 of Ref. [6], see also references therein. It follows that the results presented in these articles show the strong octupole effect in  $Z \approx 106$  with  $N \approx 196$  and  $Z \approx 120$  with  $N \approx 190$ , and correspond well with our calculations in Fig. 10.

Systematic studies of pear-shape deformation in neutron-rich actinide and superheavy nuclei in Ref. [7] confirmed again the presence of the sought effects in  $Z \approx 96$  and  $N \approx 196$  region, but did not confirm in the area of  $Z \geq 108$ . In contrast, our calculations show the presence of the rich octupole effects also in the region of nuclei surrounding those with proton number  $Z = 124$  and neutrons in the neighborhood of  $N = 196$ , cf. Fig. 11.

As far as tetrahedral symmetry goes, the results in Ref. [11] reporting the presence of  $\alpha_{32} \neq 0$  minima in  $Z = 106$  and  $N = 190$  to 192 as well as  $Z = 126$  with  $N \approx 192$  nuclei show a good correspondence with the results of our calculations presented in this article, indicating also the presence of the tetrahedral symmetry zone in  $Z \approx 98$  with  $N \approx 192$ .

There seem to be no systematic predictions in the literature addressing the  $\alpha_{33}$  effects, thus pointing to the  $D_{3h}$  symmetry comparable to our results visible in Figs. 10 and 11, bottom parts.

Let us mention in passing that, whereas the results cited above can be seen as representing various manifestations of octupole effects in nuclei and in a way as parts of various projects, our calculations can be seen as based on the common root and manifesting the specific role of the fourfold universal magic octupole  $N = 196$  effect. From this perspective, our predictions can be seen as expressing the common microscopic mechanism contributed by the  $\Delta\ell = 3 = \Delta j$  octupole-octupole repulsion over the  $N = 196$  universal octupole magic gap. From this viewpoint, such a repulsion is contributed to principally by four neutron couples viz.:  $1k_{17/2} \leftrightarrow 2h_{11/2}$  and  $1j_{13/2} \leftrightarrow 2g_{7/2}$  together with  $3f_{7/2} \leftrightarrow 4s_{1/2}$  and  $2h_{9/2} \leftrightarrow 3d_{3/2}$ , as discussed earlier in Sec. III-A, cf. Table II.

#### IV. OVERVIEW OF THE PREDICTED SHAPE EFFECTS AND THEIR EVOLUTION

We proceed illustrating in a synthetic manner nuclear shape variations with proton and neutron numbers in an attempt of deducing the roles of various spherical-harmonics as well as the evolution and possible appearance and disappearance of exotic symmetries throughout the nuclear chart. We begin with the traditional leading quadrupole and hexadecapole components  $\alpha_{20}$  and  $\alpha_{40}$  illustrated in Figs. 12 and 13, respectively.

In reference to the self-explanatory Fig. 12, let us notice two characteristic aspects. First, note the dominating quadrupole axial deformations corresponding to oblate shapes. Some of the discussed nuclei can be qualified as superdeformed oblate: those with  $\alpha_{20} \approx -0.50$  or so, whereas a few others are hyperoblate, with  $\alpha_{20} \approx -0.80$ . Second, there is a spherical ( $\alpha_{20} \approx 0$ ) area coinciding with the ensemble

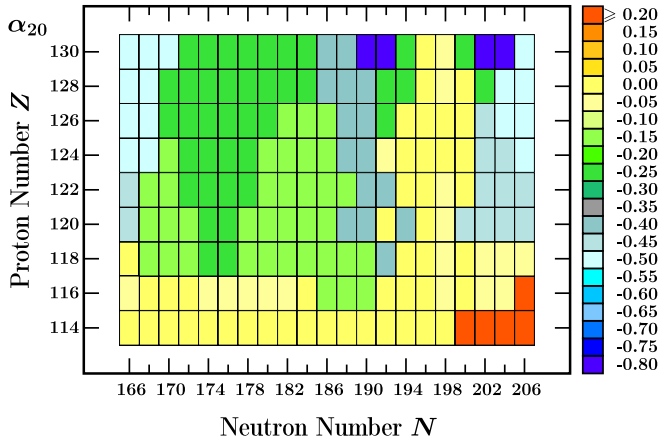


FIG. 12. Predicted  $\alpha_{20}$  ground-state quadrupole deformations obtained within the nuclear chart zone  $114 \leq Z \leq 130$  together with  $166 \leq N \leq 206$ .

of nuclei in the vicinity of  $N = 196$  fourfold magic number, where the dominating ground-state shapes correspond to exotic point-group symmetries—often with pure octupole deformations.

Figure 13 shows the distribution of accompanying hexadecapole deformations in the considered ground states. Let us notice that, whereas hexadecapole deformations lie principally in the interval  $\alpha_{40} \in [-0.10, +0.10]$ , nearly half of the values correspond to approximately vanishing  $\alpha_{40} \approx 0$ .

We proceed to overviewing the evolution of octupole shape component  $\alpha_{3\mu}$ -contributions presented in Fig. 14. Illustration shows the impact of the four octupole degrees of freedom on the stability of the superheavy nuclei in the studied zone of the nuclear landscape.

The corresponding comparison begins with the effects of the octupole pear-shape  $\alpha_{30} \neq 0$  deformations shown on top of Fig. 14, as indicated. The pear-shape deformations lie principally in the zone  $\alpha_{30} \in [0.10, 0.15]$  in nuclei with  $Z \in [114, 124]$  and  $N$  in the vicinity of 196.

The impact of the nonaxial octupole shape effects represented by  $\alpha_{31}$  deformation is shown on the diagram second

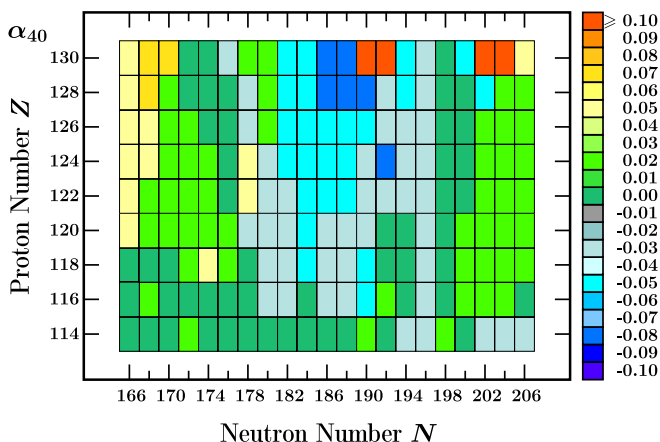


FIG. 13. Similar to the preceding one but for ground-state hexadecapole deformation  $\alpha_{40}$ .

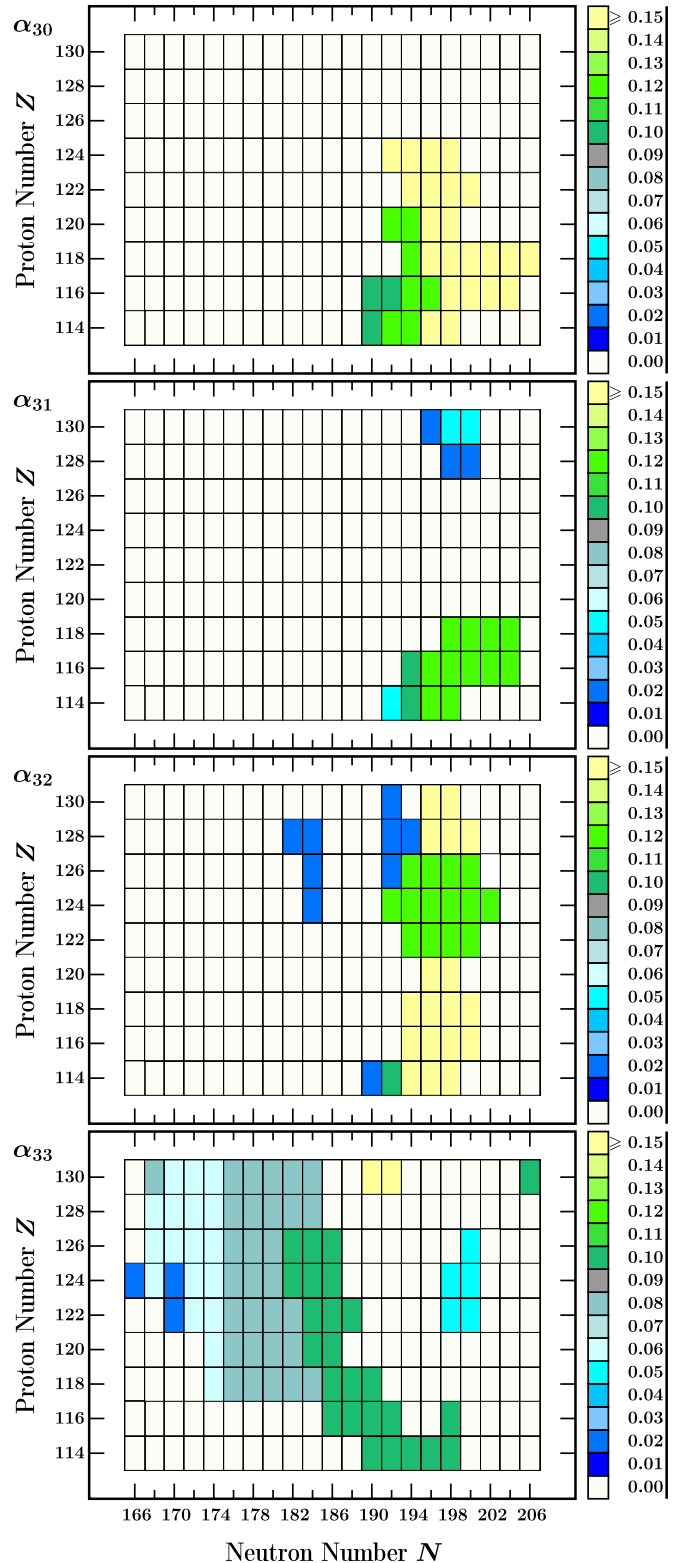


FIG. 14. From top to bottom: predicted appearance of the octupole components  $\alpha_{30}$ ,  $\alpha_{31}$ ,  $\alpha_{32}$ , and  $\alpha_{33}$  in the ground-state deformations obtained from three-dimensional mesh calculations projected on  $(\alpha_{20}, \alpha_{3\mu})$  planes after minimization over hexadecapole deformation  $\alpha_{40}$ . Observe the dominating coupling of the  $D_{3h}$ -symmetry  $\alpha_{33}$  components with the oblate quadrupole shape visible from comparison with Fig. 12.

from the top. The latter indicates at the same time the nuclei with the  $C_{2v}$  point-group symmetry, forming two islands, one with  $Z \approx 114$  and another one with  $Z \approx 130$ .

By far the strongest nonaxial octupole symmetry instabilities are generated by  $\alpha_{32}$  deformation leading to pure tetrahedral  $T_d$  point group symmetry, or, when combined with quadrupole-axial  $\alpha_{20}$  shape admixtures, leading to the  $D_{2d}$  point-group symmetry. The discussed mechanisms are concentrated mainly in the isotones of  $N \in [192, 200]$ , as seen from Fig. 14, third diagram.

A specific behavior among nonaxial octupole shapes is manifested by  $\alpha_{33}$  deformation leading to  $D_{3h}$  point-group symmetry with characteristic three-fold symmetry axis among elements of this group. There are two observations which need mentioning. First,  $\alpha_{33}$  is present in the equilibrium deformations of nearly half of the nuclei in the zone of the nuclear chart considered in this project, thus dominating among the four types of octupole shapes. The second observation relates to the combination of this information with the one contained in Fig. 12 indicating that in the majority of the nuclei considered here, the  $\alpha_{33} \neq 0$  components combine with  $\alpha_{20} < 0$ , i.e., oblate deformation of non-negligible size.

It will be instructive to analyze the stability properties of the octupole ground-state minima presented so far, Fig. 15. This can be done by employing as the first criterion, a comparison of the energies of the states in question and the nearest competing excited minimum at non-zero quadrupole deformation, the latter in the majority of the cases corresponding to vanishing octupole deformations. Another, more direct criterion of stability is provided by the heights of potential-energy barriers between the two types of minima just mentioned, Fig. 16.

The properties of the total energy maps—regarding the first of the above criteria—are very characteristic, cf. Fig. 7. Indeed one can observe that double minima related to the octupole-type symmetry are accompanied by the axial symmetry minima with  $\alpha_{3\mu} = 0$  and  $\alpha_{20} < 0$ , the latter of the order of  $\alpha_{20} \approx -0.25$ . Comparison of the relative energies of those two minima provides a direct estimate of the energy gain between the states with exotic symmetries at  $\alpha_{3\mu} \neq 0$  and the quadrupole deformed competing partner minima with  $\alpha_{3\mu} = 0$ .

Let us emphasize that such a comparison becomes impracticable in a number of cases with the energy landscapes resembling those in Fig. 6, cf. the  $\alpha_{30}$  and  $\alpha_{31}$  projections for  $^{310}\text{Fl}$ , where the role of the single oblate shape minima mentioned is played by slightly-higher-lying but still double-octupole minima, with both the octupole and the quadrupole deformations nonvanishing. It turns out that, for  $\alpha_{31}$ -projection, this will be the case for all nuclei studied in this project, whereas in the case of the other three projections, only some nuclei present the lack of quadrupole minimum. This is also why in the illustrations in Figs. 15 and 16 the  $\alpha_{31}$ -projection is totally missing.

After these introductory observations, let us summarize the information about the energy gains due to the octupole deformations  $\alpha_{30}$ ,  $\alpha_{32}$ , and  $\alpha_{33}$ . The corresponding information is collected in Fig. 15, in the form of chessboard plots, presenting energy differences  $E(\alpha_{20}, \alpha_{3\mu} = 0) - E(\alpha_{20}, \alpha_{3\mu} \neq 0)$

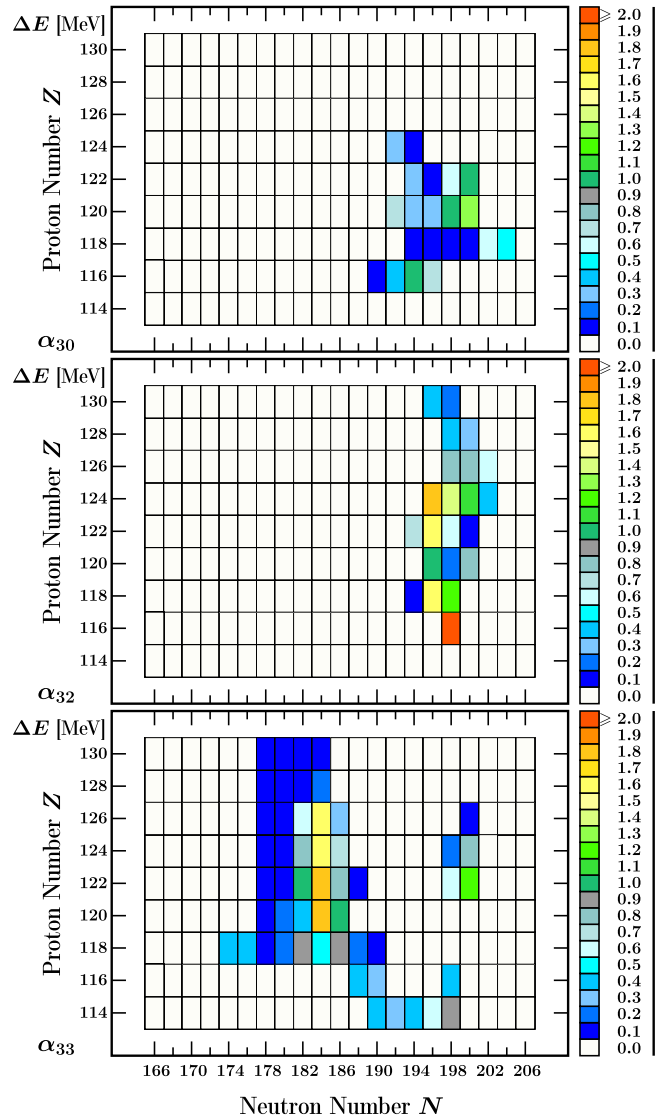


FIG. 15. From top to bottom: the predicted energy differences between the nearest quadrupole-shape minimum (with  $\alpha_{3\mu} = 0$ ) and the indicated octupole-deformed configuration  $\alpha_{30}$ ,  $\alpha_{32}$ , and  $\alpha_{33}$  in the ground-state deformations obtained from three-dimensional mesh calculations projected on  $(\alpha_{20}, \alpha_{3\mu})$  planes after minimization over hexadecapole deformation  $\alpha_{40}$ .

with the three corresponding diagrams as indicated. According to this convention, the displayed energies are positive. One can summarize by saying that the energy gains due to the discussed octupole deformations do not bypass the limits of the order of  $\Delta E \approx 2$  MeV.

Using analogous graphical convention, in Fig. 16 we present the collection of the barrier heights separating octupole shape twin-minima from those with the pure axial quadrupole shape introduced earlier in relation to the results in Fig. 15. In the majority of the cases the discussed separating barriers remain within the range between 1.5 and 2.5 MeV above the octupole deformed ground states, only in a very few cases the limit of 3 MeV is bypassed.

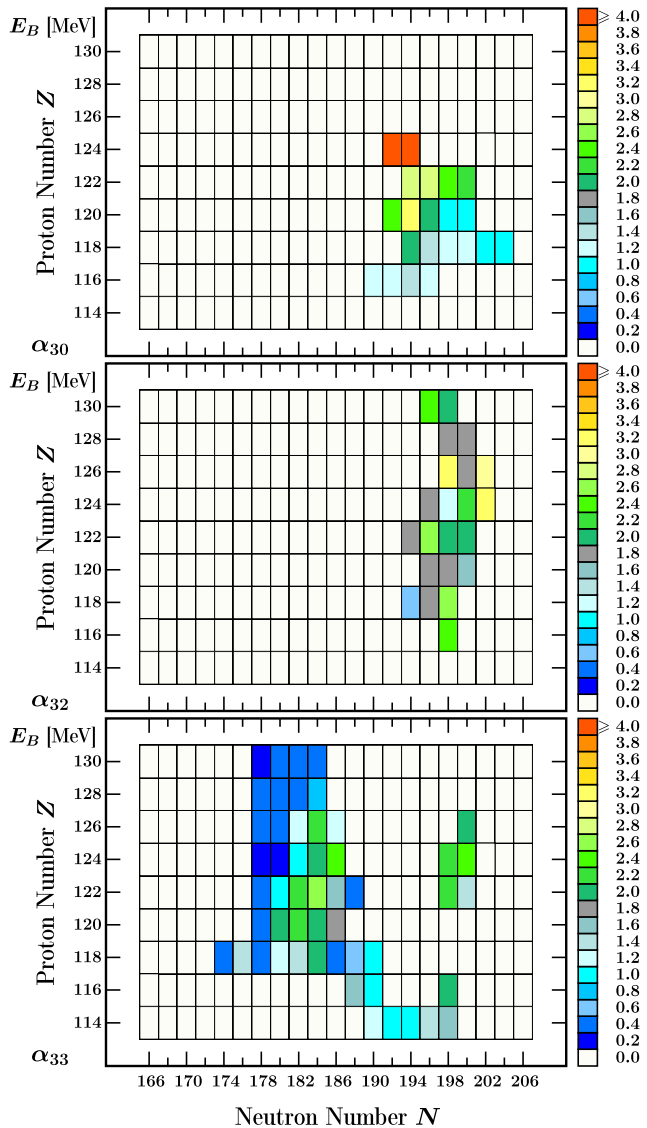


FIG. 16. From top to the bottom: Predicted barrier heights between the nearest quadrupole-shape minimum (with  $\alpha_{3\mu} = 0$ ) and the indicated octupole-deformed configuration  $\alpha_{30}$ ,  $\alpha_{32}$ , and  $\alpha_{33}$  obtained from three-dimensional mesh calculations projected on  $(\alpha_{20}, \alpha_{3\mu})$  planes after minimization over hexadecapole deformation  $\alpha_{40}$ .

## V. COMPARING SELECTED UNIVERSAL PARAMETERIZATIONS OF THE WOODS-SAXON POTENTIAL

Adjustment of parameters of theoretical modeling by employing stochastic methods of inverse problem theory of *applied mathematics* is a technique more and more often employed today. It facilitates, at the same time, examining uncertainties of model predictions. In the past, more elementary means of addressing uncertainties and stability of model predictions by directly comparing the results of alternative Hamiltonian parametrizations were often used, for instance parametrizations obtained using different experimental data sets. Within the present project, an instructive test of this kind

would consist in comparing Hamiltonian parametrizations based on experimental single-particle energies from spherical, as opposed to deformed nuclei, and we will follow this line as one of the possibilities.

At this point we address uncertainties of modeling with our Hamiltonian by comparing results with various types of parameter sets corresponding either to different time periods (thus in particular to different qualities of the experimental data sets) or to nonequivalent ways of extracting the experimental information. It turns out that it will be possible for us to combine both types of comparisons by considering the time stretches of over 40 years between the variants of “universal parametrization,” whereas illustrating at the same time the impact of adjustments to experimental single-particle levels extracted from the spherical-nuclei vs deformed-nuclei data sets.

### A. Stability of predictions related to octupole deformations

In this section we would like to address a comparison of the nuclear shell energies as functions of nuclear octupole deformations,  $\alpha_{30}$ ,  $\alpha_{31}$ ,  $\alpha_{32}$ , and  $\alpha_{33}$ , for three different parametrizations just introduced.

We begin by comparing in Fig. 17 the results for three selections of parameter sets of the phenomenological Woods-Saxon potential serving as universal, i.e., applicable to all nuclei in the nuclear chart. They are referred to as *Parametrization 1* (in the latter case the parameters were optimized to reproduce the information about experimental single-particle levels in deformed nuclei, Ref. [46]), followed by *Parametrization 2* (based on Ref. [48] in which case the experimental information about single-particle levels in spherical nuclei was used), and the recent *Parametrization 3* based on the results from Ref. [44], discussed and commented in several places in the present article.

Compared with the results in Fig. 17, the curves in Fig. 18 indicate clearly that the impact of the numbers of protons is limited to the interval of the octupole deformation around the origin of the reference frame,  $\alpha_{30} \in [-0.2, +0.2]$ , and this for all the three parametrizations. Outside of this interval all curves approximately coincide, which manifests the independence of the results of the proton numbers. The combined dependence on the neutron number and  $\alpha_{30}$  is qualitatively similar, but there are systematic differences in the quantitative level. This applies particularly to the results with the newest parametrization compared with the oldest ones, cf. top and middle diagrams vs the bottom one in Fig. 17.

Very similar observations can be made about the shell-energy behavior as function of the first nonaxial deformation  $\alpha_{31}$  shown in Figs. 19 and 20. Let us remark the similarities in the details of deformation dependence between the curves in Figs. 17 and 19 on the one side and Figs. 18 and 20 on the other.

Arriving at the tetrahedral symmetry deformation  $\alpha_{32}$  in Figs. 21 and 22, we notice two characteristic features. First, the qualitative behavior of the compared curves can be considered very similar within the sequence of three diagrams illustrating  $Z = 114$  configurations on the one hand and the three diagrams illustrating the  $N = 196$  configurations on

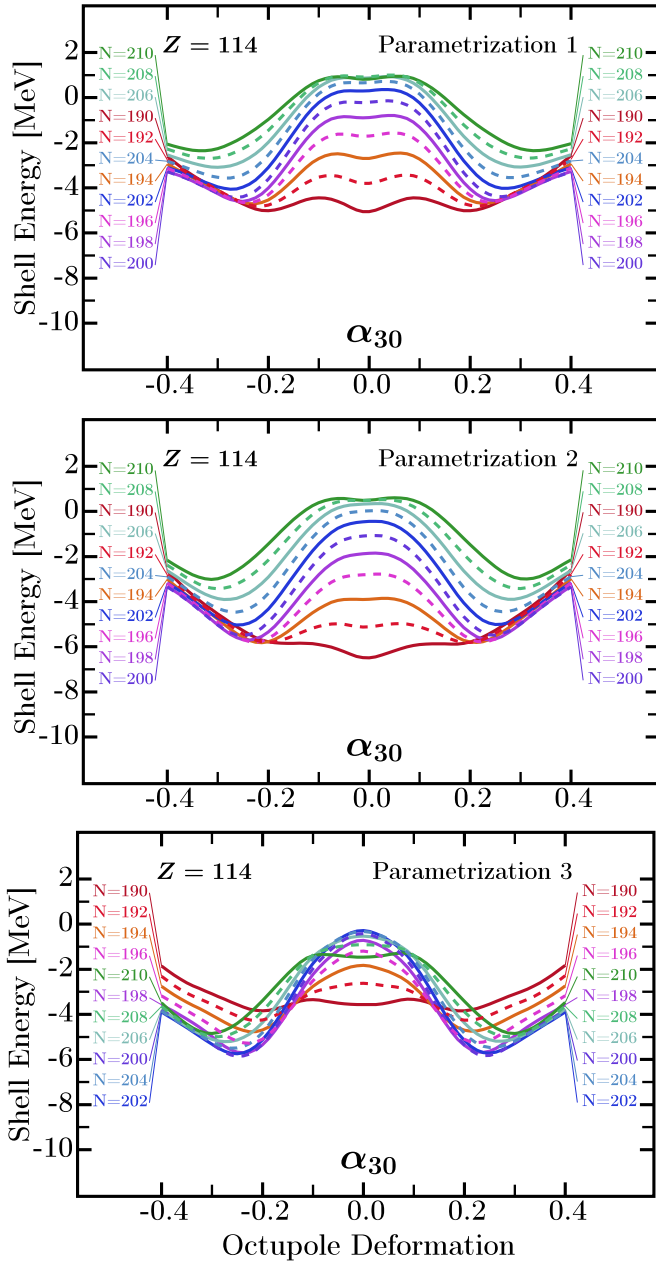


FIG. 17. Comparison of the nuclear shell-energies with varying number of neutrons for fixed proton number  $Z = 114$  as functions of pear-shape octupole deformation parameter  $\alpha_{30}$ . “Parametrization 1” based on Ref. [46] employs the experimental input from deformed nuclei, whereas “Parametrization 2,” [48] from spherical ones, and finally “Parametrization 3,” the newest one, employs the modern treatment with parametric correlation removal [44].

the other, whereas the groups differ. However, the amplitudes of variations between the neighboring extreme points visible in all the diagrams are 30% to 50% larger in the  $\alpha_{32}$  case as compared with all the other deformations. This, as mentioned earlier has to do with the presence of four-dimensional irreducible representations of the double tetrahedral group,  $T_d^D$ , the symmetry group of the mean-field *fermion* Hamiltonian.

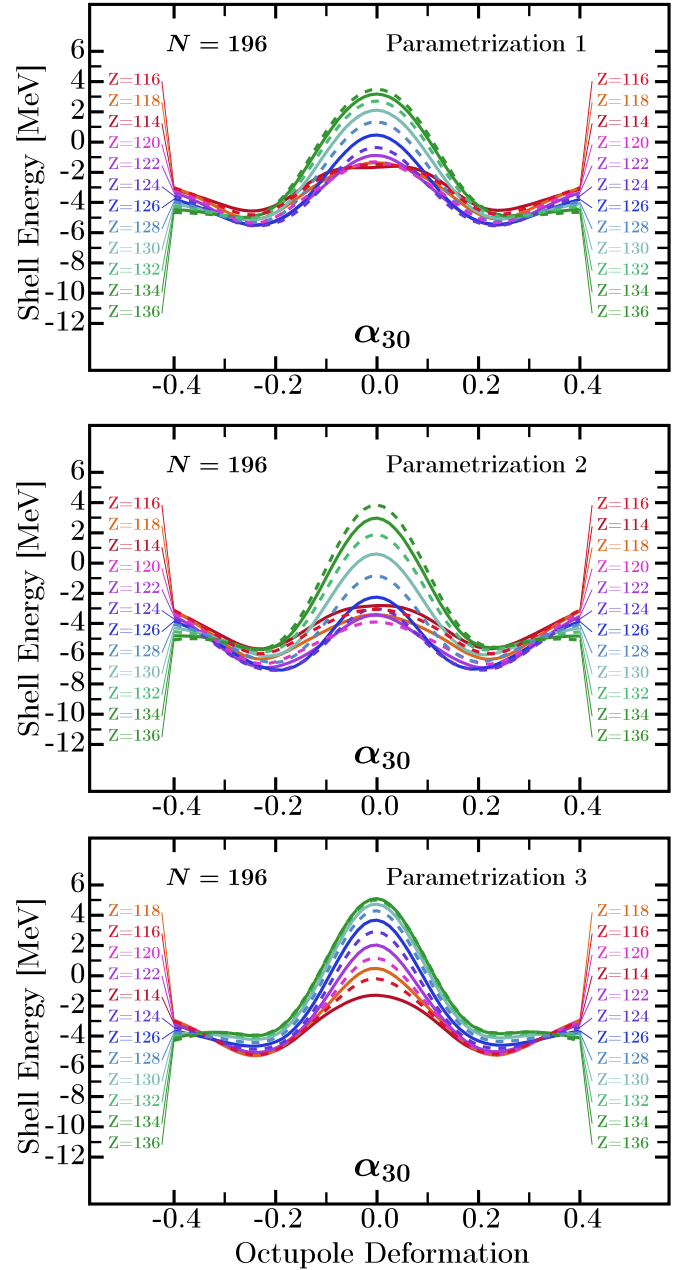


FIG. 18. Similar to the preceding one but comparing the shell energies with varying number of protons at fixed neutron number  $N = 196$  as functions of the octupole deformation  $\alpha_{30}$ . For further comments see caption to Fig. 17.

Referring to  $\alpha_{33}$  deformation, the last in the sequence, all that has been said about the preceding cases can be repeated at this point, both concerning the similarities between the  $Z = 114$  curves among themselves and the  $N = 196$  curves among themselves, and systematic differences when comparing the two sets.

To summarize: Illustrations in Figs. 17–24 show striking robustness of the Hamiltonian through far-reaching similarities of total shell energy curves despite the differences in the experimental sources used to extract the parameters considered optimal in each given context.

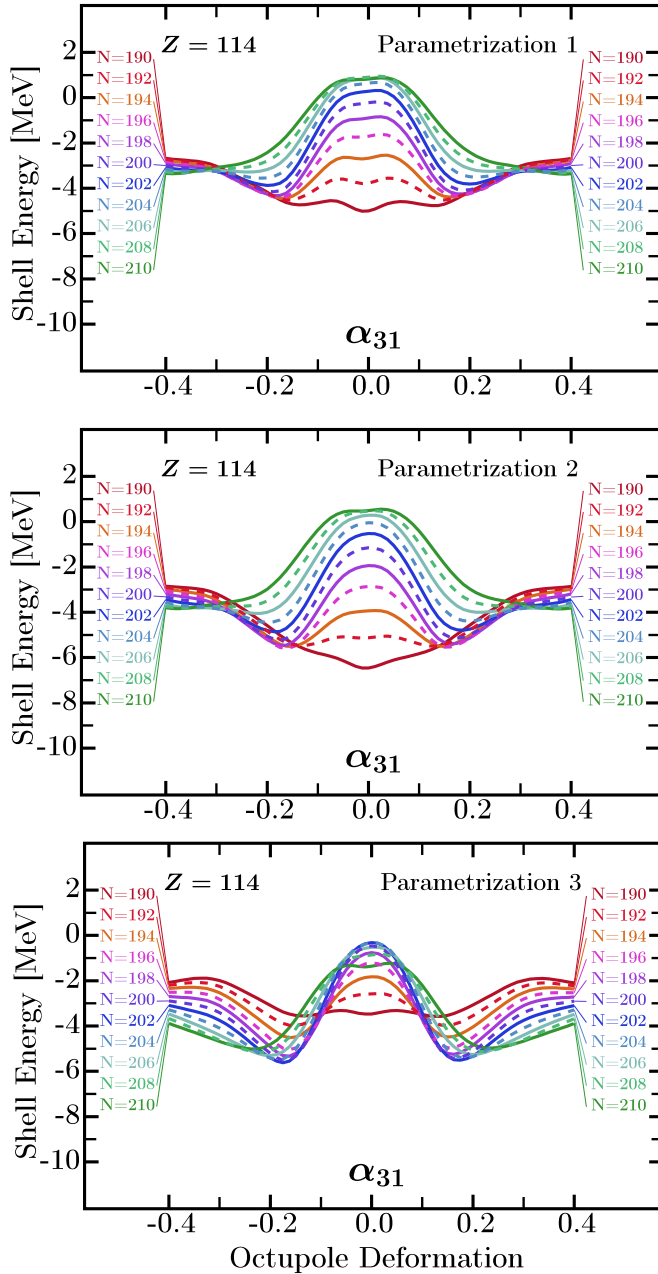


FIG. 19. Similar to illustration in Fig. 17, i.e., shell energies for varying  $N$  but for the nonaxial octupole deformation  $\alpha_{31}$  at fixed  $Z = 114$ .

### B. Stability of predictions related to elongation

Finally, let us present the shell effects illustrated in Figs. 25 and 26 and the underlying single-particle spectra shown in Fig. 27, here focusing separately on the neutron and proton effects as functions of the nuclear elongation, quadrupole deformation  $\alpha_{20}$ . In contrast with the preceding illustrations where we addressed the octupole deformation driving mechanisms around octupole magic number  $N = 196$ , here we confront the neutron and proton single-particle spectra with shell energies.

Let us emphasize again that the similarities among the shell energies corresponding to the three compared parametriza-

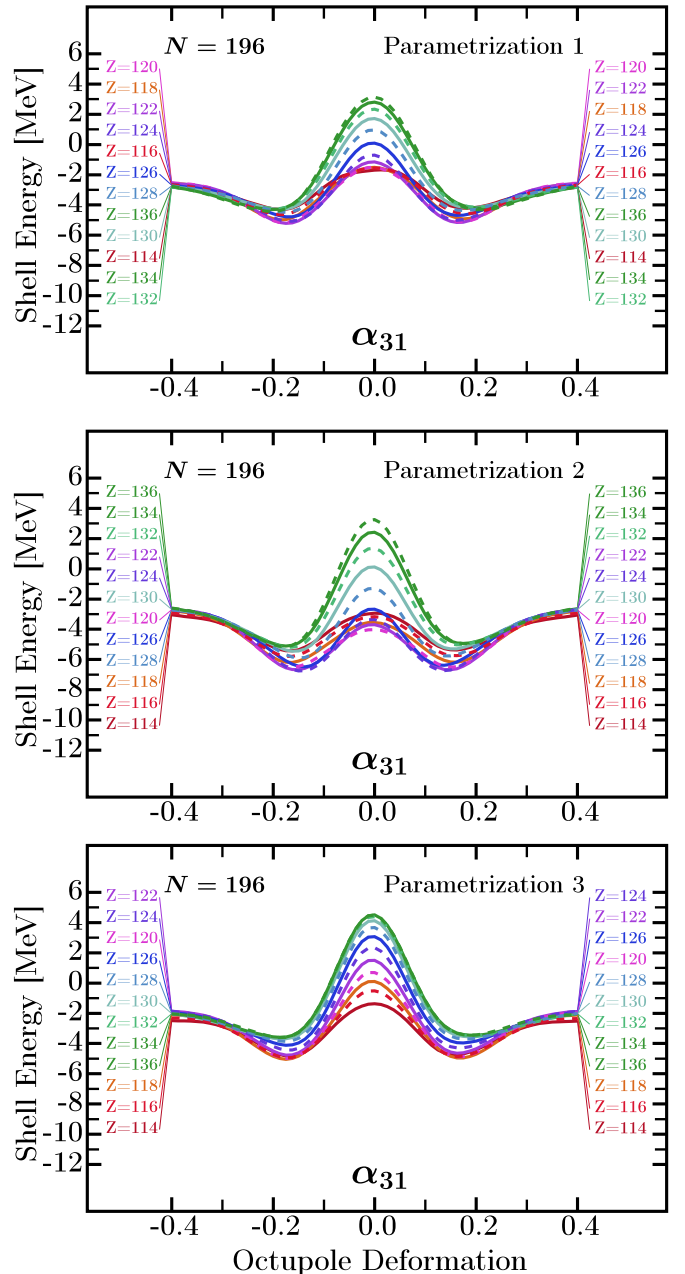


FIG. 20. Analogous to the preceding one with the exchanged roles of protons and neutrons, here at fixed neutron number  $N = 196$ .

tions visible in Figs. 25 and 26 are far-reaching, especially as Parametrizations 1 and 2 are concerned, for which even details in the curve variations remain nearly the same. The results corresponding to Parametrization 3 keep very close quantitative resemblance to the two preceding ones, once again signaling what we refer to as a robustness of the modeling: It is not true that one could be afraid of that different parametrizations lead to dramatically different or opposite theory predictions.

To terminate the discussion we present the single-particle neutron energies as functions of the quadrupole deformation, Fig. 27, corresponding to the results in the preceding two figures. Understandably, the single-nucleon spectra generated by the compared parametrizations are similar and we restrict

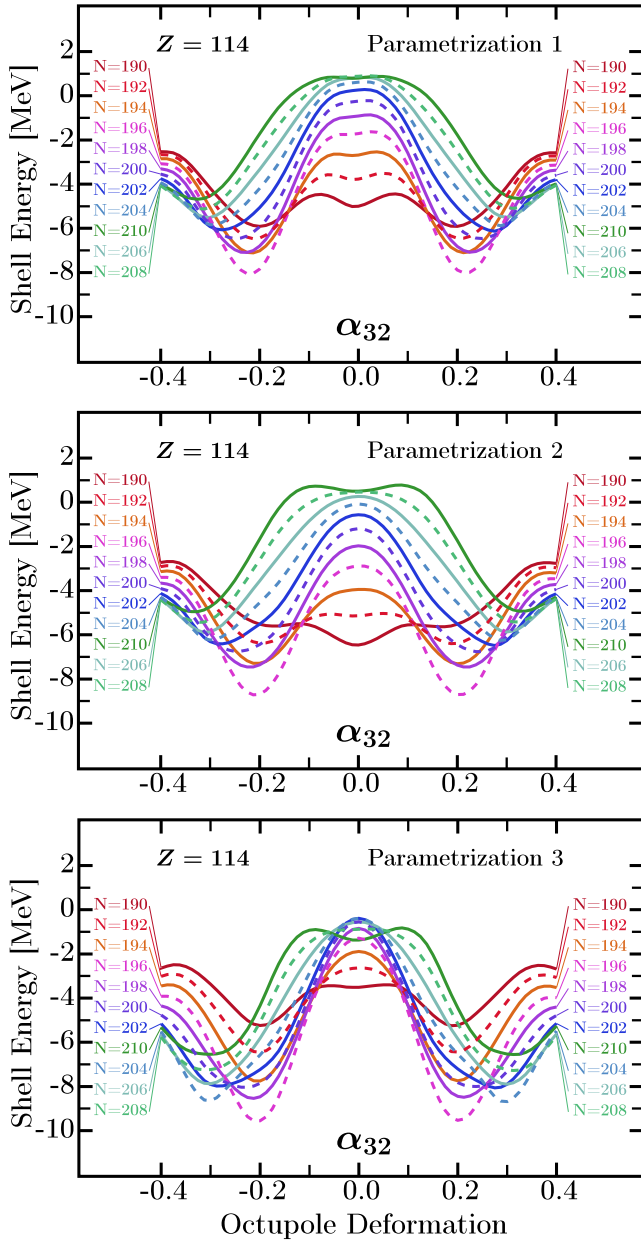


FIG. 21. Similar to preceding ones but for the shell energies with increasing neutron number at fixed  $Z = 114$  for varying tetrahedral symmetry deformation  $\alpha_{32}$ .

ourselves to presenting the case of the newest one, from Ref. [44]. As mentioned earlier in this article the diagrams like those shown here represent many levels in the relatively narrow energy windows, which makes it difficult to attribute particular importance to one gap or the other. This being said, one can still distinguish the propagation of, in particular, the high- $j$  orbitals over the presented energy windows, and this despite the relatively broad  $\alpha_{20}$  deformation stretch.

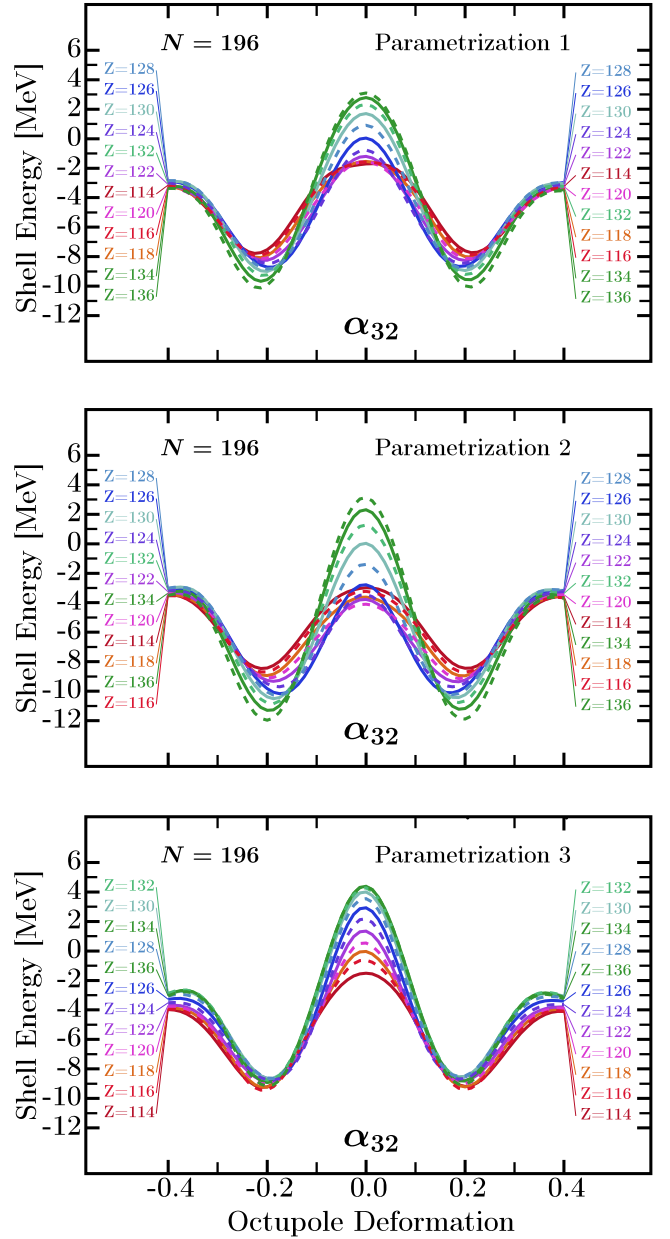


FIG. 22. Analogous to the preceding one with varying proton number at fixed neutron one at  $N = 196$ , as functions of  $\alpha_{32}$ .

### C. Parameterizations and their comparisons: Comments about different ways of comparing

We would like to add a few observations to complete our section devoted to the problem of robustness of the Hamiltonian used in the present project and the stability of its predictions of the evolution of nuclear shapes and symmetries. These issues were illustrated by comparing the results of, in principle, nonequivalent parameterizations. We wish to address specifically the question of parameterizations optimized to the experimental data related to spherical, as opposed to deformed, nuclei.

It is well known that certain single-particle levels in spherical nuclei strongly couple to the collective surface-oscillations

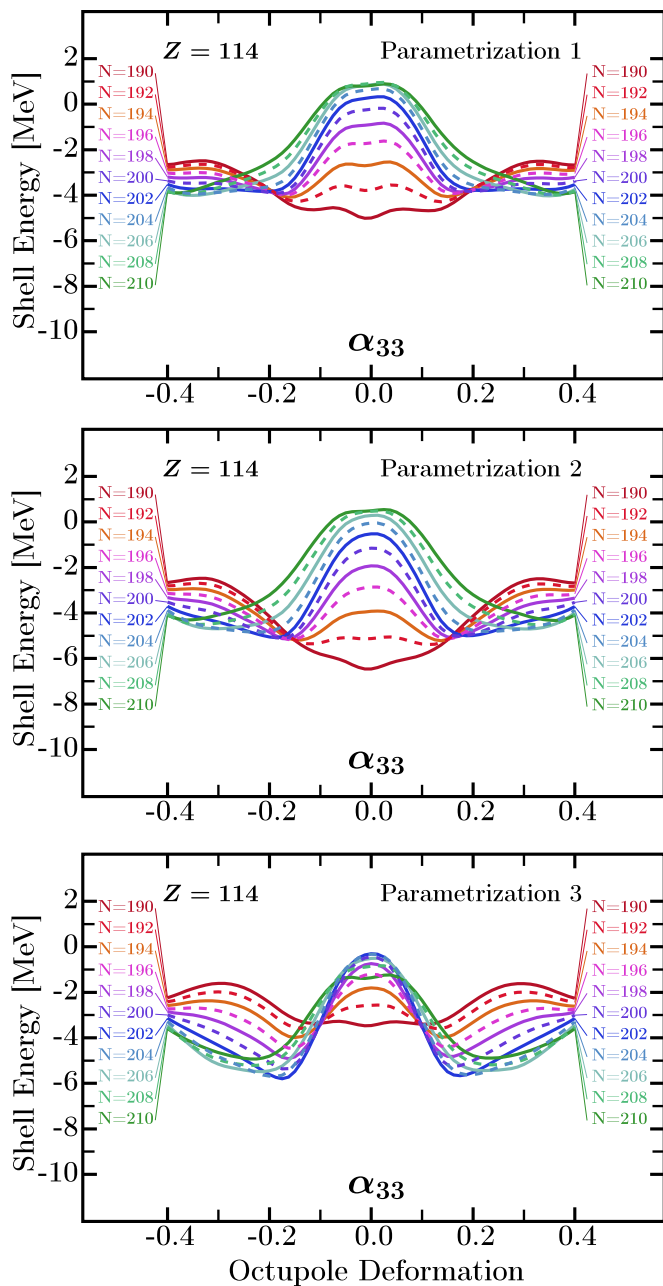


FIG. 23. The final illustration completing the sequence of Figs. 17, 19, 21, showing the shell energies for varying neutron number, here for  $D_{3h}$ -symmetry-generating deformation  $\alpha_{33}$  at  $Z = 114$ .

generated by the low-energy quadrupole or octupole vibrations. This type of coupling should be taken into account within model-dependent procedures of extraction of what is referred to as *experimental single-particle energies*.

The reader should recall at this point that the concept of an isolated single-particle motion introduced in the mean-field theory discussions by statements like “consider a free motion of a nucleon in a deformed *mean* field without interactions” is a mathematical abstraction. All measured effects are contributed to by all nuclear interactions simultaneously. Consequently, comparisons between single-particle effects

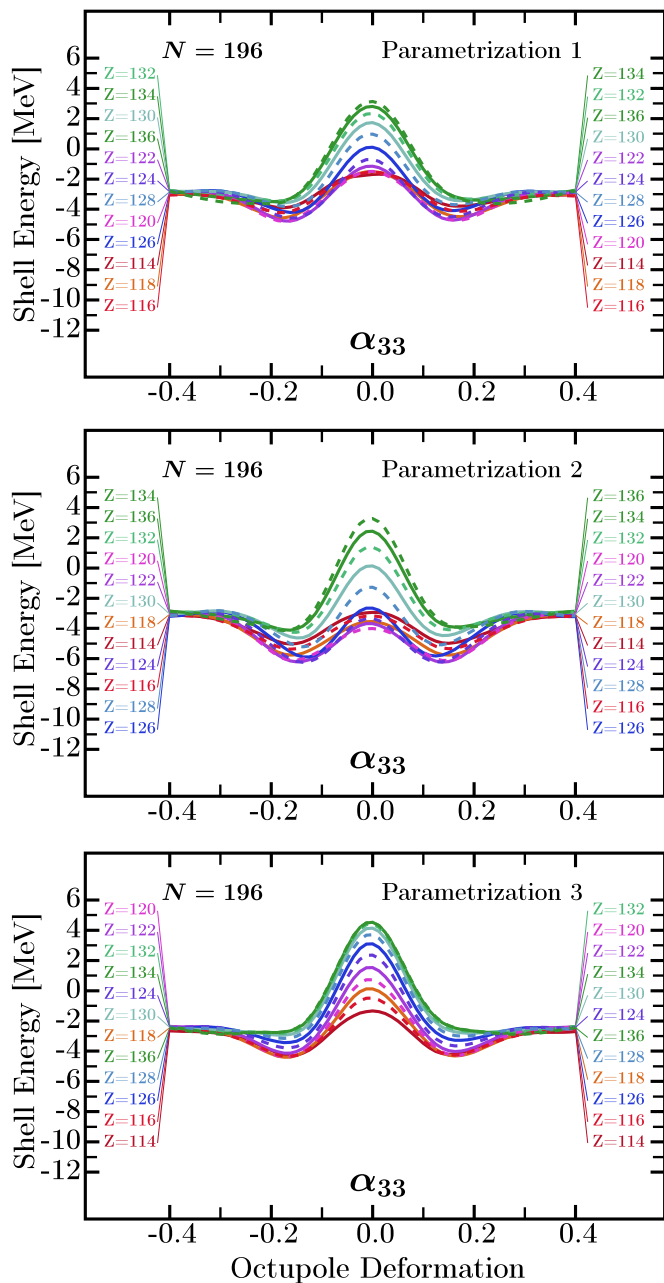


FIG. 24. Partner illustration for the preceding one. It completes the sequence of Figs. 18, 20, 22 with the shell energies for varying proton number and deformation  $\alpha_{33}$  at fixed neutron magic number  $N = 196$ .

obtained within the mean-field theory and experiment is and has always been based on model-dependent algorithms within which one is trying to model and extract the energies representing the free nucleonic motion, cf. e.g., Sec. 2 in Ref. [51]. It then follows that, if the experimental single-particle energy extraction algorithms take into account vibration coupling as a leading perturbing mechanism in spherical nuclei, the so-obtained information should be consistent with that obtained from the deformed ones. In this way we may argue that the effect of coupling of the single-particle states with vibrations have been in a way “subtracted” and the so-obtained exper-

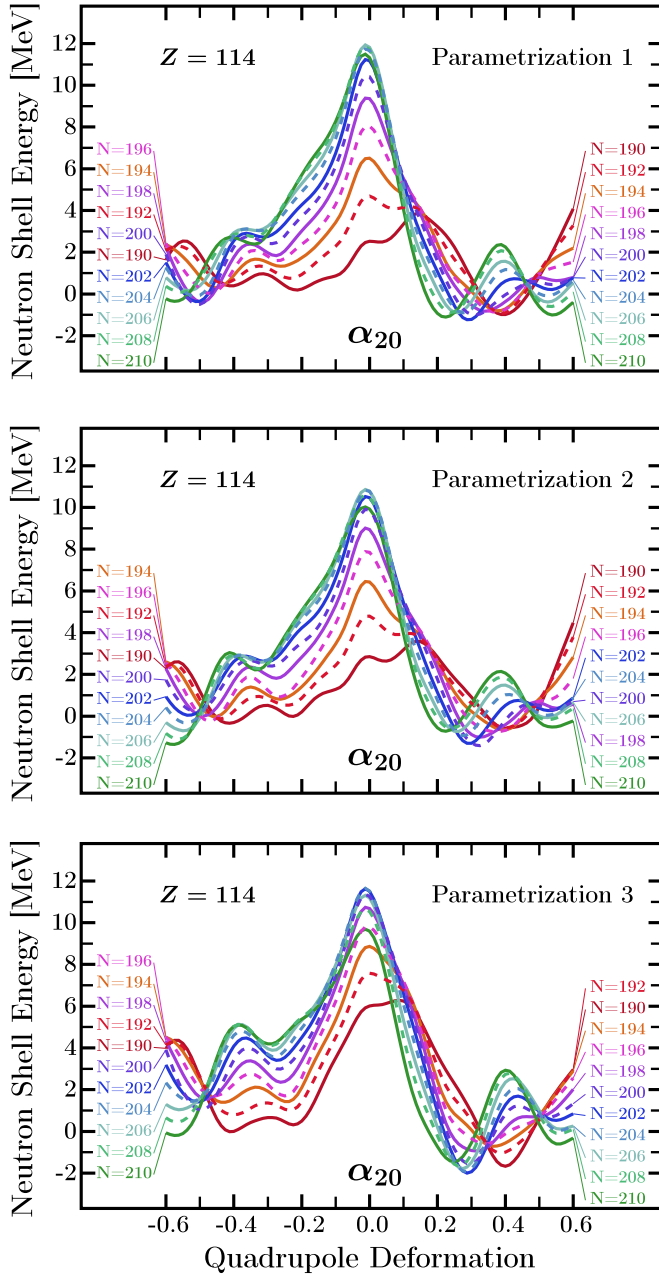


FIG. 25. Neutron shell energies as functions of the quadrupole elongation  $\alpha_{20}$  and neutron number for  $Z = 114$  and for the three parametrizations introduced in the text: Partner illustration to the one in Fig. 27, top.

imental single-particle energies should be comparable with pure mean-field ones.

Under these circumstances, i.e., with the appropriate techniques of extraction of the single nucleon energies out of the experimental data bases on either spherical or deformed nuclei—taking into account the perturbing effects of coupling with shape oscillations—one may expect that the comparison with theory will not depend in any essential manner on the parametrization used since the energies of the vibration-coupling were “subtracted out.” Indeed, all the

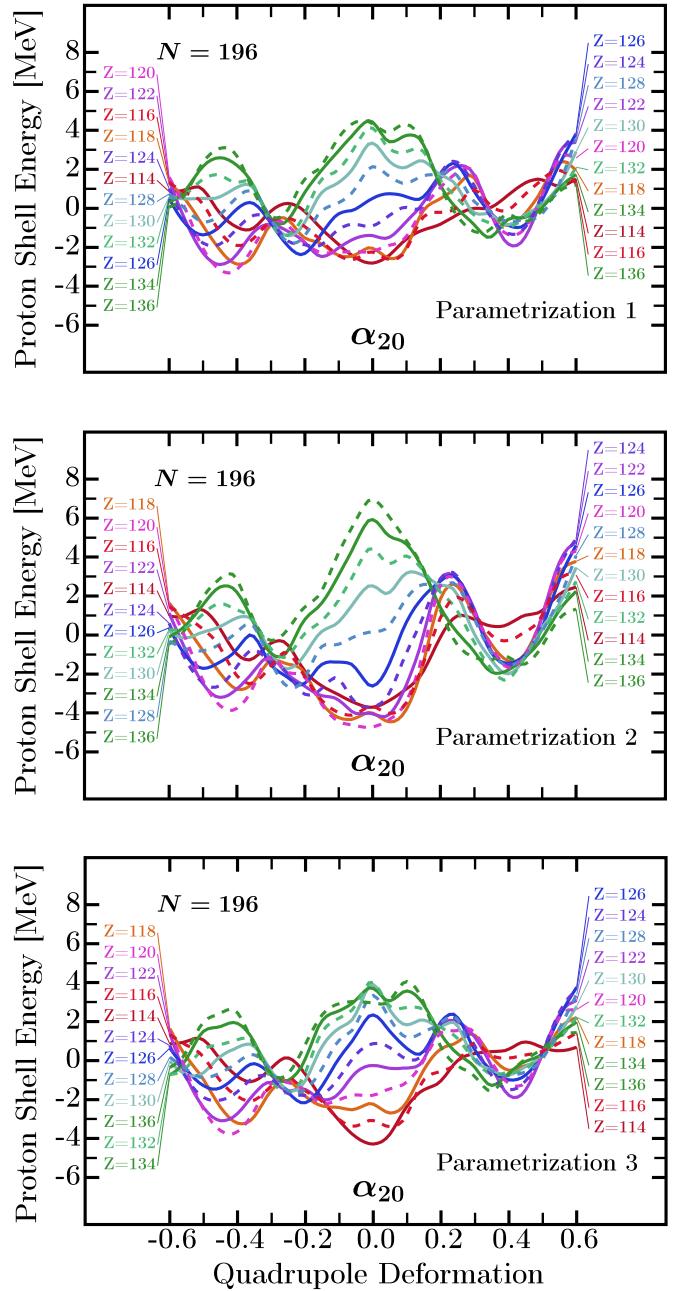


FIG. 26. Analogous to the preceding one but for proton shell energies with varying  $\alpha_{20}$  and the proton number at fixed  $N = 196$ ; to be compared with Fig. 27, bottom.

results presented in the present section confirm these expectations.

## VI. SUMMARY AND CONCLUSIONS

This article is devoted to examining the impact of exotic geometrical symmetries associated with the octupole degrees of freedom on the stabilization of superheavy nuclei in the mass range limited by  $114 \leq Z \leq 130$  and  $166 \leq N \leq 206$ . This mass range selection was guided by the idea of covering the area of the nuclear landscape, in which the symmetries

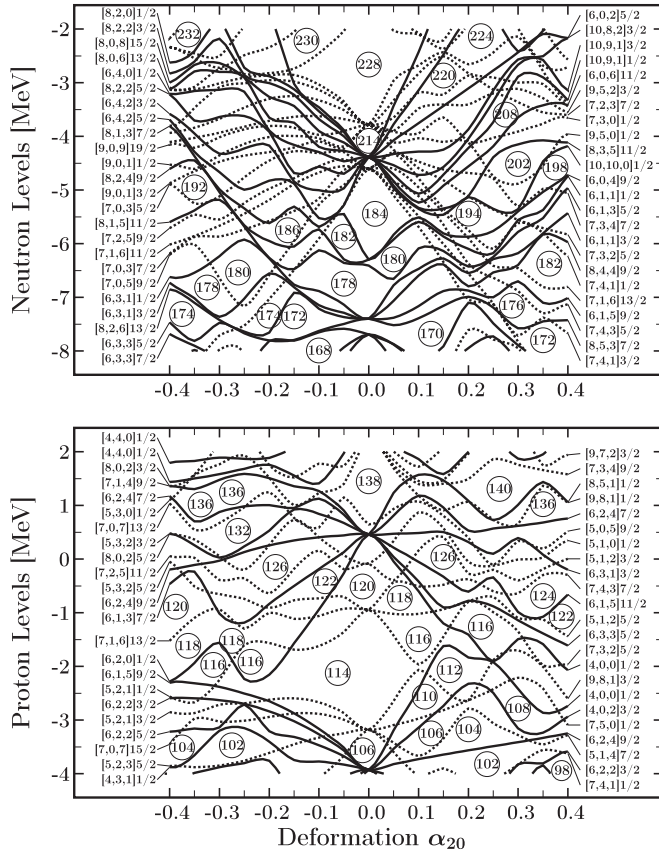


FIG. 27. Quadrupole deformation dependence of the single-particle levels for the neutrons, top, and the protons, bottom, characteristic for all the three parametrizations presented in previous figures. Here we employed the newest parametrization, Ref. [44], which, given the equivalence of the deduced shell energies nearly independent of the parametrization—as discussed in the text—can be considered representative for all the three. The central nucleus is chosen to correspond to the center of the  $(Z, N)$ -zone addressed in this article:  $Z_0 = 122$  and  $N_0 = 186 \leftrightarrow (114 \leq Z \leq 130$  and  $166 \leq N \leq 206)$ .

in question were predicted by our mean-field calculations. Indeed, extending our recent studies of the symmetry-induced nuclear stability of heavy nuclei in the lead and actinide regions, Ref. [3], we have discovered an existence of the universal, fourfold octupole magic number  $N = 196$ , an analog of the similar fourfold, i.e., applying to all four octupole deformations  $\alpha_{30}$ ,  $\alpha_{31}$ ,  $\alpha_{32}$ , and  $\alpha_{33}$ , magic number  $N = 136$ . The latter was shown to importantly stabilize the mentioned lighter nuclei.

To study the stability properties of the selected superheavy nuclei we employed the phenomenological nuclear mean-field approach using the deformed Woods-Saxon potential with its universal (i.e., applying simultaneously to all nuclei in the nuclear chart) parametrization together with the standard macroscopic-microscopic method. Parameter optimization of the corresponding Hamiltonian has been recently completed in Ref. [44], following the rules of the *inverse problem theory* of applied mathematics combined with Monte Carlo simulations. The presence of parametric correlations among 4

parameters generated by the original set of 12 of the Hamiltonian has been detected. These correlations were removed applying Monte Carlo approach. Removal, according to the well-known general theorems of inverse problem theory, leads to stabilization of the corresponding theoretical predictions and increases the predictive capacities of the corresponding Hamiltonian and implied modeling, according to stochastic arguments.

As the starting-point test we have verified that the spherical shell gaps at proton number  $Z = 114$  and the neutron numbers  $N = 164, 184, 228$ , and  $258$  predicted earlier by other authors are obtained employing our optimized parametrization without extra adjustments. We believe that this supports extending our calculations with removed parametric correlations to superheavy nuclei and argues in favor of their predictive capacities. The uncertainty distributions of single-particle level positions for protons and neutrons are presented. Results indicate that the FWHM values increase with the orbital angular momentum and vary, typically, between about 200 keV for the  $s_{1/2}$  and 450 keV for the  $k_{17/2}$  levels.

The octupole shell effects and the underlying single-nucleon energy-gap structures and shell energies are analyzed in detail. Among four octupole deformations,  $\alpha_{30}$ ,  $\alpha_{31}$ ,  $\alpha_{32}$ , and  $\alpha_{33}$ , the tetrahedral one ( $\alpha_{32}$ ) manifests the strongest shell effects at neutron number  $N = 196$ . These strong neutron shell effects are accompanied by weaker octupole shell effects at proton numbers  $Z = 106, 116$ , and  $124$ . The corresponding impacts in terms of the intensity of the effect expressed by the depth of the potential-energy minima and heights of the separating potential barriers are illustrated and discussed. We associate the origin of the underlying particularly strong single-nucleon energy-gap structures with the special group-theory properties of the  $T_d^D$  tetrahedral double group: The presence of four-dimensional irreducible representations and associated fourfold degeneracies of single-particle levels.

Let us observe that the size of the single-particle tetrahedral gap at  $N = 196$  is comparable to the size of the spherical gap at  $N = 184$ , both of the order of 2 MeV. This signifies that the exotic (tetrahedral) shape-symmetry generates shell effects comparable with the strongest ones known so far in the studied nuclei.

Let us emphasize that certain point groups with nonaxial symmetry are predicted to generate numerous isomeric configurations. For instance, the tetrahedral symmetry hinders emission of collective electric-quadrupole ( $E2$ ) and electric-dipole ( $E1$ ) transitions just increasing the chances that low-lying excited states lead to measurable lifetimes. One may expect that the full class of particle-hole excitations will be carrying the mentioned symmetries and generating isomers, some of which could become measurable.

## ACKNOWLEDGMENTS

J.D., H-L.W., and J.Y. would like to acknowledge partial support by the Polish National Science Centre under Contract No. 2016/21/B/ST2/01227. H-L.W. acknowledges partial support from the National Natural Science Foundation of China (Grant No. 11975209) and the Physics Research and

Development Program of Zhengzhou University (Grant No. 32410017). Partial support from French-Polish collaboration

COPIN, No. 04-113 and No. 05-119 and COPIGAL is acknowledged.

- [1] Information extracted from the NuDat database 2022, National Nuclear Data Center (NNDC), <https://www.nndc.bnl.gov/nudat/>.
- [2] Yu. Ts. Oganessian, *J. Phys. G* **34**, R165 (2007).
- [3] J. Yang, J. Dudek, I. Dedes, A. Baran, D. Curien, A. Gaamouci, A. Gózdź, A. Pędrak, D. Rouvel, H. L. Wang, and J. Burkat, *Phys. Rev. C* **105**, 034348 (2022).
- [4] J. Dudek, D. Curien, I. Dedes, K. Mazurek, S. Tagami, Y. R. Shimizu, and T. Bhattacharjee, *Phys. Rev. C* **97**, 021302(R) (2018).
- [5] S. E. Agbemava, A. V. Afanasjev, and P. Ring, *Phys. Rev. C* **93**, 044304 (2016).
- [6] S. E. Agbemava and A. V. Afanasjev, *Phys. Rev. C* **96**, 024301 (2017).
- [7] A. Afanasjev, H. Abusara, and S. Agbemava, *Phys. Scr.* **93**, 034002 (2018).
- [8] Y. Cao, S. E. Agbemava, A. V. Afanasjev, W. Nazarewicz, and E. Olsen, *Phys. Rev. C* **102**, 024311 (2020).
- [9] P. Möller, J. Nix, W. Myers, and W. Swiatecki, *At. Data Nucl. Data Tables* **59**, 185 (1995).
- [10] M. Warda and J. L. Egido, *Phys. Rev. C* **86**, 014322 (2012).
- [11] P. Jachimowicz, M. Kowal, and J. Skalski, *Phys. Rev. C* **95**, 034329 (2017).
- [12] P. Jachimowicz, M. Kowal, and J. Skalski, *At. Data Nucl. Data Tables* **138**, 101393 (2021).
- [13] S. Hofmann and G. Münzenberg, *Rev. Mod. Phys.* **72**, 733 (2000).
- [14] K. Morita, K. Morimoto, D. Kaji, T. Akiyama, S. Goto, H. Haba, E. Ideguchi, K. Katori, H. Koura, H. Kikunaga, H. Kudo, T. Ohnishi, A. Ozawa, N. Sato, T. Suda, K. Sueki, F. Tokanai, T. Yamaguchi, A. Yoneda, and A. Yoshida, *J. Phys. Soc. Jpn.* **73**, 2593 (2004).
- [15] Yu. Ts. Oganessian, V. K. Utyonkov, Yu. V. Lobanov, F. Sh. Abdullin, A. N. Polyakov, I. V. Shirokovsky, Yu. S. Tsyganov, G. G. Gulbekian, S. L. Bogomolov, B. N. Gikal, A. N. Mezentsev, S. Iliev, V. G. Subbotin, A. M. Sukhov, G. V. Buklanov, K. Subotic, M. G. Itkis, K. J. Moody, J. F. Wild, N. J. Stoyer, M. A. Stoyer, and R. W. Loughheed, *Phys. Rev. Lett.* **83**, 3154 (1999).
- [16] Yu. Ts. Oganessian, V. K. Utyonkov, Yu. V. Lobanov, F. Sh. Abdullin, A. N. Polyakov, I. V. Shirokovsky, Yu. S. Tsyganov, G. G. Gulbekian, S. L. Bogomolov, A. N. Mezentsev, S. Iliev, V. G. Subbotin, A. M. Sukhov, A. A. Voinov, G. V. Buklanov, K. Subotic, V. I. Zagrebaev, M. G. Itkis, J. B. Patin, K. J. Moody, J. F. Wild *et al.*, *Phys. Rev. C* **69**, 021601(R) (2004).
- [17] Yu. Ts. Oganessian, V. K. Utyonkov, Yu. V. Lobanov, F. Sh. Abdullin, A. N. Polyakov, R. N. Sagaidak, I. V. Shirokovsky, Yu. S. Tsyganov, A. A. Voinov, G. G. Gulbekian, S. L. Bogomolov, B. N. Gikal, A. N. Mezentsev, S. Iliev, V. G. Subbotin, A. M. Sukhov, K. Subotic, V. I. Zagrebaev, G. K. Vostokin, M. G. Itkis *et al.*, *Phys. Rev. C* **74**, 044602 (2006).
- [18] Yu. Ts. Oganessian, F. Sh. Abdullin, P. D. Bailey, D. E. Benker, M. E. Bennett, S. N. Dmitriev, J. G. Ezold, J. H. Hamilton, R. A. Henderson, M. G. Itkis, Yu. V. Lobanov, A. N. Mezentsev, K. J. Moody, S. L. Nelson, A. N. Polyakov, C. E. Porter, A. V. Ramayya, F. D. Riley, J. B. Roberto, M. A. Ryabinin *et al.*, *Phys. Rev. Lett.* **104**, 142502 (2010).
- [19] Yu. Ts. Oganessian, V. K. Utyonkov, Yu. V. Lobanov, F. Sh. Abdullin, A. N. Polyakov, R. N. Sagaidak, I. V. Shirokovsky, Yu. S. Tsyganov, A. A. Voinov, A. N. Mezentsev, V. G. Subbotin, A. M. Sukhov, K. Subotic, V. I. Zagrebaev, S. N. Dmitriev, R. A. Henderson, K. J. Moody, J. M. Kenneally, J. H. Landrum, D. A. Shaughnessy *et al.*, *Phys. Rev. C* **79**, 024603 (2009).
- [20] V. Zagrebaev and W. Greiner, *Phys. Rev. C* **78**, 034610 (2008).
- [21] V. I. Zagrebaev and W. Greiner, *Phys. Rev. C* **83**, 044618 (2011).
- [22] M. G. Mayer, *Phys. Rev.* **74**, 235 (1948).
- [23] A. Sobiczewski, F. Gareev, and B. Kalinkin, *Phys. Lett.* **22**, 500 (1966).
- [24] D. Vautherin and D. Brink, *Phys. Rev. C* **5**, 626 (1972).
- [25] S. Ćwiok, W. Nazarewicz, and P. H. Heenen, *Phys. Rev. Lett.* **83**, 1108 (1999).
- [26] K. Rutz, M. Bender, T. Bürvenich, T. Schilling, P. G. Reinhard, J. A. Maruhn, and W. Greiner, *Phys. Rev. C* **56**, 238 (1997).
- [27] R. K. Gupta, S. Patra, and W. Greiner, *Mod. Phys. Lett. A* **12**, 1727 (1997).
- [28] S. Patra, W. Greiner, and R. K. Gupta, *J. Phys. G* **26**, L65 (2000).
- [29] S. E. Agbemava, A. V. Afanasjev, T. Nakatsukasa, and P. Ring, *Phys. Rev. C* **92**, 054310 (2015).
- [30] M. Bender, W. Nazarewicz, and P. G. Reinhard, *Phys. Lett. B* **515**, 42 (2001).
- [31] A. Afanasjev, S. Agbemava, and A. Gyawali, *Phys. Lett. B* **782**, 533 (2018).
- [32] S. E. Agbemava, A. V. Afanasjev, A. Taninah, and A. Gyawali, *Phys. Rev. C* **99**, 034316 (2019).
- [33] S. E. Agbemava and A. V. Afanasjev, *Phys. Rev. C* **103**, 034323 (2021).
- [34] A. Sobiczewski and K. Pomorski, *Prog. Part. Nucl. Phys.* **58**, 292 (2007).
- [35] Y. T. Oganessian and V. Utyonkov, *Rep. Prog. Phys.* **78**, 036301 (2015).
- [36] S. Hofmann, S. Heinz, R. Mann, J. Maurer, G. Münzenberg, S. Antalic, W. Barth, H. G. Burkhard, L. Dahl, K. Eberhardt, R. Grzywacz, J. H. Hamilton, R. A. Henderson, J. M. Kenneally, B. Kindler, I. Kojouharov, R. Lang, B. Lommel, K. Miernik, D. Miller *et al.*, *Eur. Phys. J. A* **52**, 180 (2016).
- [37] S. Hofmann, *EPJ Web Conf.* **182**, 02054 (2018).
- [38] L. A. Malov, G. G. Adamian, N. V. Antonenko, and H. Lenske, *Phys. Rev. C* **104**, 064303 (2021).
- [39] V. M. Strutinsky, *Nucl. Phys. A* **95**, 420 (1967); **122**, 1 (1968).
- [40] M. Brack, J. Damgaard, A. S. Jensen, H. C. Pauli, V. M. Strutinsky, and C. Y. Wong, *Rev. Mod. Phys.* **44**, 320 (1972).
- [41] H. J. Krappe, J. R. Nix, and A. J. Sierk, *Phys. Rev. C* **20**, 992 (1979).
- [42] P. Möller and J. R. Nix, *Nucl. Phys. A* **361**, 117 (1981).
- [43] P. Möller and J. R. Nix, *At. Data Nucl. Data Tables* **26**, 165 (1981).
- [44] A. Gaamouci, I. Dedes, J. Dudek, A. Baran, N. Benhamouda,

- D. Curien, H. L. Wang, and J. Yang, *Phys. Rev. C* **103**, 054311 (2021).
- [45] J. Dudek and T. Werner, *J. Phys. G: Nucl. Phys.* **4**, 1543 (1978).
- [46] J. Dudek, A. Majhofer, J. Skalski, T. Werner, S. Cwiok, and W. Nazarewicz, *J. Phys. G: Nucl. Phys.* **5**, 1359 (1979).
- [47] J. Dudek, W. Nazarewicz, and T. Werner, *Nucl. Phys. A* **341**, 253 (1980).
- [48] J. Dudek, Z. Szymański, and T. Werner, *Phys. Rev. C* **23**, 920 (1981).
- [49] S. Cwiok, J. Dudek, W. Nazarewicz, J. Skalski, and T. Werner, *Comput. Phys. Commun.* **46**, 379 (1987).
- [50] To illustrate the use-frequency of the “universal” Woods-Saxon phenomenological mean-field Hamiltonian we quote below the articles which appeared only in one year (2013) and only in one journal: J. Rissanen, R. M. Clark, K. E. Gregorich, J. M. Gates, C. M. Campbell, H. L. Crawford *et al.*, *Phys. Rev. C* **88**, 044313 (2013); W. Brodziński and J. Skalski, *ibid.* **88**, 044307 (2013); S. Lalkowski, A. M. Bruce, A. M. Denis Bacelar, M. Górska, S. Pietri, Z. Podolyak *et al.*, *ibid.* **88**, 024302 (2013); H. L. Liu and F. R. Xu, *ibid.* **87**, 067304 (2013); D. S. Delion and R. J. Liotta, *ibid.* **87**, 041302(R) (2013); D. S. Delion, R. J. Liotta, and R. Wyss, *ibid.* **87**, 034328 (2013); D. S. Delion and J. Suhonen, *ibid.* **87**, 024309 (2013); D. Deleanu, D. L. Balabanski, T. Venkova, D. Bucurescu, N. Mărginean, E. Ganioglu *et al.*, *ibid.* **87**, 014329 (2013).
- [51] J. Dudek, B. Szpak, M.-G. Porquet, H. Molique, K. Rybak, and B. Fornal, *J. Phys. G* **37**, 064031 (2010).
- [52] The Editors, *Phys. Rev. A* **83**, 040001 (2011).
- [53] J. Dudek, *Acta Phys. Polon. B* **9**, 919 (1978).
- [54] I. Dedes and J. Dudek, *Phys. Rev. C* **99**, 054310 (2019).
- [55] J. Blomqvist and S. Wahlborn, *Ark. Fys.* **16**, 543 (1960).
- [56] V. A. Chepurinov, *Yad. Fiz.* **6**, 955 (1967).
- [57] E. Rost, *Phys. Lett. B* **26**, 184 (1968).
- [58] A. V. Afanasjev, S. E. Agbemava, D. Ray, and P. Ring, *Phys. Rev. C* **91**, 014324 (2015).
- [59] A. Taninah, S. E. Agbemava, and A. V. Afanasjev, *Phys. Rev. C* **102**, 054330 (2020).
- [60] I. Hamamoto, B. Mottelson, H. Xie, and X. Z. Zhang, *Z. Phys. D: At. Mol. Clusters* **21**, 163 (1991).